



**AFRL-OSR-VA-TR-2013-0455**

**PERIDYNAMIC MODELING OF FRACTURE AND FAILURE OF  
MATERIALS**

**ERDOGAN MADENCI**

**UNIVERSITY OF ARIZONA**

**08/09/2013  
Final Report**

**DISTRIBUTION A: Distribution approved for public release.**

**AIR FORCE RESEARCH LABORATORY  
AF OFFICE OF SCIENTIFIC RESEARCH (AFOSR)/RSA  
ARLINGTON, VIRGINIA 22203  
AIR FORCE MATERIEL COMMAND**

REPORT DOCUMENTATION PAGE				Form Approved OMB No. 0704-0188	
Public reporting burden for this collection of information is estimated to average 1 hour per response, including the time for reviewing instructions, searching existing data sources, gathering and maintaining the data needed, and completing and reviewing this collection of information. Send comments regarding this burden estimate or any other aspect of this collection of information, including suggestions for reducing this burden to Department of Defense, Washington Headquarters Services, Directorate for Information Operations and Reports (0704-0188), 1215 Jefferson Davis Highway, Suite 1204, Arlington, VA 22202-4302. Respondents should be aware that notwithstanding any other provision of law, no person shall be subject to any penalty for failing to comply with a collection of information if it does not display a currently valid OMB control number. <b>PLEASE DO NOT RETURN YOUR FORM TO THE ABOVE ADDRESS.</b>					
1. REPORT DATE (DD-MM-YYYY) 02-08-2013		2. REPORT TYPE Final report		3. DATES COVERED (From - To) (01-03-2010)-(30-04-2013)	
4. TITLE AND SUBTITLE PERIDYNAMIC MODELING OF FRACTURE AND FAILURE OF MATERIALS				5a. CONTRACT NUMBER FA9550-10-1-0200	
				5b. GRANT NUMBER	
				5c. PROGRAM ELEMENT NUMBER	
6. AUTHOR(S) Erdogan Madenci				5d. PROJECT NUMBER	
				5e. TASK NUMBER	
				5f. WORK UNIT NUMBER	
7. PERFORMING ORGANIZATION NAME(S) AND ADDRESS(ES) Aerospace and Mechanical Engineering Department The University of Arizona Tucson, AZ 85721-4108				8. PERFORMING ORGANIZATION REPORT NUMBER	
9. SPONSORING / MONITORING AGENCY NAME(S) AND ADDRESS(ES) Air Force Office of Scientific Research 875 North Randolph Street Suite 325, Room 3112 Arlington, VA 22203-1768				10. SPONSOR/MONITOR'S ACRONYM(S) AFOSR	
				11. SPONSOR/MONITOR'S REPORT NUMBER(S)	
12. DISTRIBUTION / AVAILABILITY STATEMENT Unlimited					
13. SUPPLEMENTARY NOTES					
14. ABSTRACT his study presents the capability of the use of the peridynamic laminate theory to capture both the failure progression and residual strength of monolithic and composite laminates. Predicting damage and residual strengths of composite materials involves capturing complex, distinct and progressive failure modes. Peridynamics is a reformulation of classical continuum mechanics that utilizes integral equations in place of partial differential equations to remove the difficulty in handling discontinuities, such as cracks or interfaces, within a body. Damage is included within the constitutive model; initiation and propagation can occur without resorting to special crack growth criteria necessary in other commonly utilized approaches. The peridynamic theory realistically models the load redistribution arising from the presence of complex failure modes through the use of multiple interaction types. This study specifically employs an inverse approach to obtain the critical peridynamic failure parameters necessary to capture the residual strength of a structure. The validity of the inverse approach is demonstrated by first considering its application in determining the residual strength of isotropic materials with pre-existing cracks. Its validity is also demonstrated by predicting failure loads and final failure					
15. SUBJECT TERMS peridynamics, composites, progressive failure					
16. SECURITY CLASSIFICATION OF:			17. LIMITATION OF ABSTRACT	18. NUMBER OF PAGES 42	19a. NAME OF RESPONSIBLE PERSON Erdogan Madenci
a. REPORT	b. ABSTRACT	c. THIS PAGE			19b. TELEPHONE NUMBER (include area code) 52-250-1399

# **PERIDYNAMIC MODELING OF FRACTURE AND FAILURE OF MATERIALS**

**Dr. Erdogan Madenci  
Aerospace and Mechanical Engineering Department  
The University of Arizona  
Tucson, AZ 85721-4108**

**Final Report  
Grant/Contract Number: FA9550-10-1-0200**

**August 2, 2013**

## Table of Contents

1. Abstract .....	3
2. Introduction .....	3
3. State-based peridynamic laminate theory .....	7
3.1. Material parameters .....	12
3.2. Numerical verification .....	14
3.2.1. Laminates subjected to tensile loading .....	15
3.2.2. Laminate with a hole subjected to tensile loading .....	23
3.2.3. Laminate subjected to three point bending .....	24
4. Failure predictions .....	26
4.1. Damage in monolithic materials .....	26
4.2 Damage in composite laminates .....	28
4.3 Inverse approach for critical stretch .....	28
4.3.1 Monolithic materials .....	29
4.3.2 Laminated composites .....	31
4.3.2.1 Laminated plate with a center hole .....	32
5. Final remarks .....	38
6. References .....	39

## **1. Abstract**

This study presents the capability of the use of the peridynamic laminate theory to capture both the failure progression and residual strength of monolithic and composite laminates. Predicting damage and residual strengths of composite materials involves capturing complex, distinct and progressive failure modes. Peridynamics is a reformulation of classical continuum mechanics that utilizes integral equations in place of partial differential equations to remove the difficulty in handling discontinuities, such as cracks or interfaces, within a body. Damage is included within the constitutive model; initiation and propagation can occur without resorting to special crack growth criteria necessary in other commonly utilized approaches. The peridynamic theory realistically models the load redistribution arising from the presence of complex failure modes through the use of multiple interaction types. This study specifically employs an inverse approach to obtain the critical peridynamic failure parameters necessary to capture the residual strength of a structure. The validity of the inverse approach is demonstrated by first considering its application in determining the residual strength of isotropic materials with pre-existing cracks. Its validity is also demonstrated by predicting failure loads and final failure modes in a laminate with various hole diameters subjected to tensile and compressive loads.

## **2. Introduction**

By utilizing failure analysis simulations that are able to capture the failure modes and structural behavior, the residual strength of structures can be accurately estimated in the design phase. Increased confidence in these simulations enables a suitable design for a structure to be realized more efficiently through the reduction in design iterations and number of experimental test required for structural validation.

The ability to accurately predict the failure of a material is perhaps one of the most important tasks within engineering, as understanding the failure load is paramount in designing a safe structure. Whereas a reasonable estimate can be safely made without understanding the complex mechanisms of fracture, lighter structures can be realized with accurate modeling that accounts for crack initiation, growth, and propagation through the media. A host of mechanisms can influence the initiation of failure, as well as the progression through a structure. Griffith (1921) investigated failure initiation in glass by using the principle of conservation of energy, which helped explain the large discrepancy between the measured stress to break glass and the theoretical stress required to break the bonds between atoms. This became the basis for the concept of Linear Elastic Fracture Mechanics (LEFM). Based on this landmark study, numerous investigations were performed to explore the fracture processes and establish criteria for predicting crack growth. Williams (1957) showed that, within the realm of classical continuum mechanics, the stress field near the crack tip approaches infinity in an elastic and isotropic material. The initiation of fracture could be correlated with a stress intensity factor to describe the singular stress field. The presence of this mathematical singularity and the need for external criteria to determine failure is problematic when considering realistic structures with complex stress fields.

Consideration of complex geometries and loading conditions requires the interjection of an external failure criteria into a suitable framework for determining how and when a defect in the form of a crack propagates. The finite element method (FEM) is robust in its ability to determine stress fields and suitable for modeling structures. Different failure criteria were incorporated into the framework of FEM with varying degrees of success. It was not until the introduction of cohesive zone elements by Hillerborg et al. (1976) for Mode-I fracture mode and Xu and Needleman (1994) for a mixed-mode fracture that a major breakthrough in computational fracture mechanics was realized. These methods are based on the cohesive zone concept independently proposed by Dugdale (1960) and Barenblatt (1962). This concept introduces a restraining stress acting across the separating surfaces to remove the stress singularity at the crack tip. Cohesive zone elements are usually surface elements that are placed along the element boundaries limiting crack growth to these regions. However, the crack paths are unknown a priori, and they are highly sensitive to mesh texture and alignment (Klein et al., 2001). The concept of eXtended Finite Element Method (XFEM) was introduced as a technique to model cracks and crack growth within the realm of finite elements without remeshing (Belytschko and Black, 1999; Moees et al., 1999). XFEM is based on the partition of unity property of finite elements (Melenk and Babuska, 1996). It permits cracks to propagate through any surface within an element, removing the limitations of the cohesive zone elements. While being successfully used to consider numerous fracture problems, the XFEM still requires external crack growth criteria to predict crack growth.

When considering failure in complex materials, such as fiber reinforced composite laminates, the existing failure criteria are phenomenological and empirical in nature. There exist two commonly accepted methods: progressive ply failure and damage mechanics. The damage mechanics approach employs physically based equations for damage initiation and evolution while considering the microstructure of material (Falzon and Apruzzese, 2011; Lapczyk and Hurtado, 2007; Talreja, 1994). However, it requires extensive material characterization for damage parameters, and in most cases such measurements are not feasible. Progressive ply failure combines failure criteria for damage type identification (Hashin, 1980; Sun, 2008) and degradation of the material stiffness (Chang and Chang, 1987; Chang and Lessard, 1991; Ochoa and Reddy, 1992). The value of degradation factor is not-physically based; it is assigned a small enough value in order to ensure the convergence of finite element analysis with traditional plate elements for modeling composite laminates.

Silling (2000) and Silling et al. (2007) introduced the peridynamic theory to remove discontinuities within classical continuum theory and to predict failure in monolithic materials. In the peridynamic (PD) theory, internal forces are expressed through nonlocal force interactions between material points within a continuous body. Each material point interacts with other material points within a finite distance referred to as the horizon, and damage is part of the constitutive model. The resulting equations of motion do not require the use spatial derivatives, and therefore, are defined even in the presence of a discontinuity.

The PD theory is a reformulation of the classical continuum equations of motion. It replaces the partial differential equations of motion with integro-differential equations. The equations of motion from classical continuum theory, can be expressed as

$$\rho(\mathbf{x})\ddot{\mathbf{u}}(\mathbf{x},t) = \nabla \cdot \boldsymbol{\sigma} + \mathbf{b}(\mathbf{x},t) \quad (1)$$

in which  $\rho$  is the mass density, and  $\boldsymbol{\sigma}$  is the first Piola-Kirchoff stress tensor. The displacement and body force density vectors are denoted by  $\mathbf{u}$  and  $\mathbf{b}$  respectively. The position vector  $\mathbf{x}$  defines each point with respect to the reference configuration at time  $t$ . In the PD theory, the divergence of the stress tensor on the right hand side of Eq. (1) is replaced with an integral that accounts for all the nonlocal force interactions that exists between a material point and all of the material points within its horizon. The PD equations of motion can be expressed in terms of the force density vector,  $\mathbf{t}$ , that exists between material points, as

$$\rho(\mathbf{x})\ddot{\mathbf{u}}(\mathbf{x},t) = \int_H (\mathbf{t}(\mathbf{u}' - \mathbf{u}, \mathbf{x}' - \mathbf{x}, t) - \mathbf{t}'(\mathbf{u} - \mathbf{u}', \mathbf{x} - \mathbf{x}', t)) dH + \mathbf{b}(\mathbf{x},t) . \quad (2)$$

where the material point  $\mathbf{x}$  interacts with material point  $\mathbf{x}'$  within its family of material points,  $H$ . Numerical solution to the resulting equations of motion can be achieved by discretizing in the form

$$\begin{aligned} \rho_{(k)}\ddot{\mathbf{u}}_{(k)} = & \sum_{j=1}^{\infty} \left[ \mathbf{t}_{(k)(j)}(\mathbf{u}_{(j)} - \mathbf{u}_{(k)}, \mathbf{x}_{(j)} - \mathbf{x}_{(k)}, t) \right. \\ & \left. - \mathbf{t}_{(k)(j)}(\mathbf{u}_{(j)} - \mathbf{u}_{(k)}, \mathbf{x}_{(j)} - \mathbf{x}_{(k)}, t) \right] V_{(j)} + \mathbf{b}_{(k)} \end{aligned} \quad (3)$$

With the inclusion of a damage parameter in the force density vector and with the removal of the difficulties related to discontinuities, damage initiates and progresses within a structure where it is energetically favorable. There is no need for any external failure criteria as with classical continuum based methods. PD has been shown to be extremely versatile in predicting damage. Silling (2003) considered the Kalthoff-Winkler experiment, in which a plate having two parallel notches is hit by an impactor, and showed that PD is able to predict the angle of crack growth observed in experiments. Impact damage, including from Charpy-V notch tests, was predicted by Silling and Askari (2004). A center cracked plate was used by Silling and Askari (2005) to show numerical convergence. Gerstle and Sau (2004) demonstrated the ability to model damage in plain and reinforced concrete structures. The ability to incorporate complex material models for stretching and tearing of a rubbery material was demonstrated by Silling and Bobaru (2005). Using this model, they were able to predict the oscillatory path of a blunt tool forced through a membrane, tearing of a membrane, and the crack growth in a membrane with a slit.

In recent years, PD theory has also been applied to predict damage in composites. Within the PD framework, the simplest approach to model a composite layer with directional

properties is achieved by assigning different material properties in the fiber and other (remaining) directions. The interactions between neighboring layers are defined by using inter-layer bonds. Askari et al. (2006) and Colavito et al. (2007a, 2007b) predicted damage in laminated composites subjected to low-velocity impact and damage in woven composites subjected to static indentation. In addition, Xu et al. (2007) considered notched laminated composites under biaxial loads. Also, Oterkus et al. (2010) demonstrated that PD analysis is capable of capturing bearing and shear-out failure modes in bolted composite lap-joints. Xu et al. (2008) analyzed the delamination and matrix damage process in composite laminates due to low-velocity impact. Recently, Askari et al. (2011) considered the effect of both high- and low-energy hail impacts against a toughened-epoxy, intermediate-modulus, carbon-fiber composite. Also, Hu et al. (2011, 2012) predicted the basic failure modes of fiber, matrix, and delamination in laminates with a pre-existing central crack under tension. The analytical derivation of the PD material parameters, including thermal loading conditions, was recently given by Oterkus and Madenci (2012). They also demonstrated the constraints on material constants due to the pair-wise interaction assumption. An alternative approach to model composites was introduced by Kilic et al. (2009) by distinguishing fiber and matrix materials based on the volume fraction. Although this approach may bring certain advantages by taking into account the inhomogeneous structure discretely, it is computationally more expensive than the homogenized approach. Oterkus et al. (2012) coupled PD with FEM to predict the failure loads in a curved, stiffened composite panel with a central slit subjected to uniaxial loading and an internal pressure. These studies demonstrate the ability of the PD theory to accurately model both the progressive damage and final failure modes of composite laminates.

As demonstrated by the aforementioned studies, the ability of PD to predict failure initiation and progression in monolithic and composite materials has been well established. However, no extensive investigations into the ability of PD to predict the residual strength of a structure exist. Paramount to predicting the residual strength of a structure using PD is the assignment of critical failure parameters. The most commonly used failure parameter in PD is the critical stretch. The stretch, which is analogous to strain in classical continuum mechanics, is monitored between PD material points. When the stretch value reaches the critical stretch then the interaction between those material points is terminated. Silling and Askari (2005) proposed equating the energy required to create a unit fracture surface in PD to the energy release rate in order to develop an analytical equation to determine the critical stretch. Alternatively, Kilic (2008) showed that for monolithic materials that the failure load for a plate with a central hole is directly proportional to the critical stretch. Based on these two concepts, this study presents an inverse approach to determine the critical stretch value required for the accurate determination of the residual strength of a structure. It applies such a method to both monolithic materials and fiber-reinforced composite laminates.



### 3 . State-based peridynamic laminate theory

Although the use of laminated composites enables the design and fabrication of advanced airframes, there exist significant design limitations on composite structures. These limitations are often related to inter-laminar stresses. Thick section laminates, especially in the transverse direction, experience high stresses as a result of bending moments, specific local stresses and impact damage. Many applications have a dynamic combination of high load/high cycle, which often results in delamination formation and crack growth. Failure of composite structures involves a progressive series of events with discrete failure modes such as matrix cracking, fiber-matrix shear, fiber breakage, and delamination. Despite the development of many important concepts to predict material behavior and failure, the prediction of failure modes and residual strength of FRP composites is still a challenge. It is evident that the inhomogeneous nature of composites must be retained in the analysis.

The peridynamic theory (PD) pertaining to monolithic materials was introduced by Silling (2000) and Silling et al (2007). Based on these studies, several different approaches to model composite laminates were proposed. In the PD theory, material points interact with each other directly through the prescribed response function, which contains all of the constitutive information associated with the material. The response function includes a length parameter called the horizon,  $\delta$ . The locality of interactions depends on the horizon, and interactions become more local with a decreasing horizon. Each fiber-reinforced composite lamina of a laminate shown in Fig. 1 is idealized as a two-dimensional structure with the directional dependency of the interactions between the PD material points. As shown in Fig. 2, the material point ( $q$ ) represents material points that interact with material point ( $k$ ) only along the fiber direction with an orientation angle of  $\theta$  in reference to the  $x$ -axis. Similarly, material point ( $r$ ) represents material points that interact with material point ( $k$ ) only along the transverse direction. However, the material point ( $p$ ) represents material points that interact with material point ( $k$ ) in any direction, including the fiber and transverse directions. The orientation of a PD interaction between the material point ( $k$ ) and the material point ( $p$ ) is defined by the angle  $\phi$  with respect to the  $x$ -axis. The domain of integration,  $H$  shown in Fig. 2 is a disk with radius  $\delta$  and thickness  $h$ . The material points in a particular lamina interact with the other material points of immediate neighboring laminae above and below it.

As shown in Fig. 1, the reference coordinate system ( $x, y, z$ ) is located on the mid-plane of the laminate. The laminate thickness,  $h$  is given by

$$h = \sum_{n=1}^N h_n \quad (4)$$

where  $N$  is the total number of lamina in the stacking sequence, and  $h_n$  is the thickness of  $n^{th}$  lamina. With respect to the mid-plane, the position of each lamina,  $z_n$  is defined as

$$z_n = -\frac{h}{2} + \sum_{m=1}^{n-1} h_m + \frac{1}{2} h_n \quad (5)$$

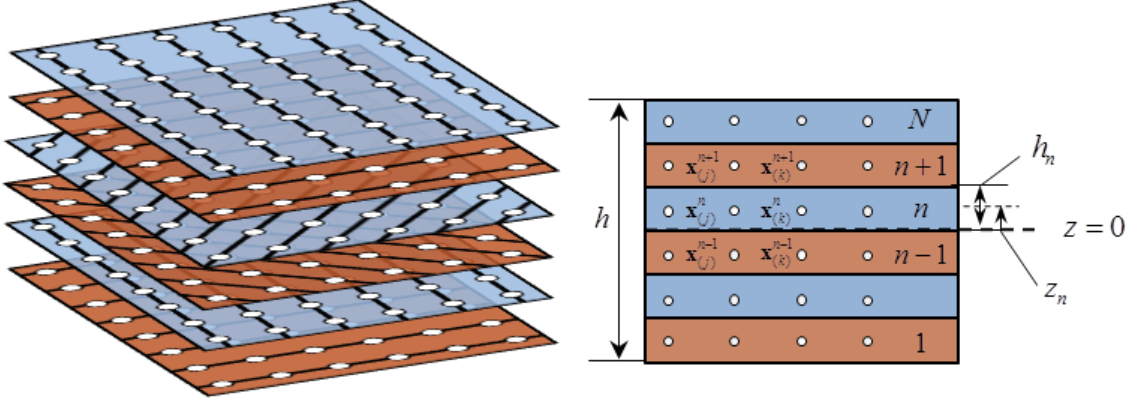


**Figure 1.** Elevation of each lamina in laminate and PD material points.

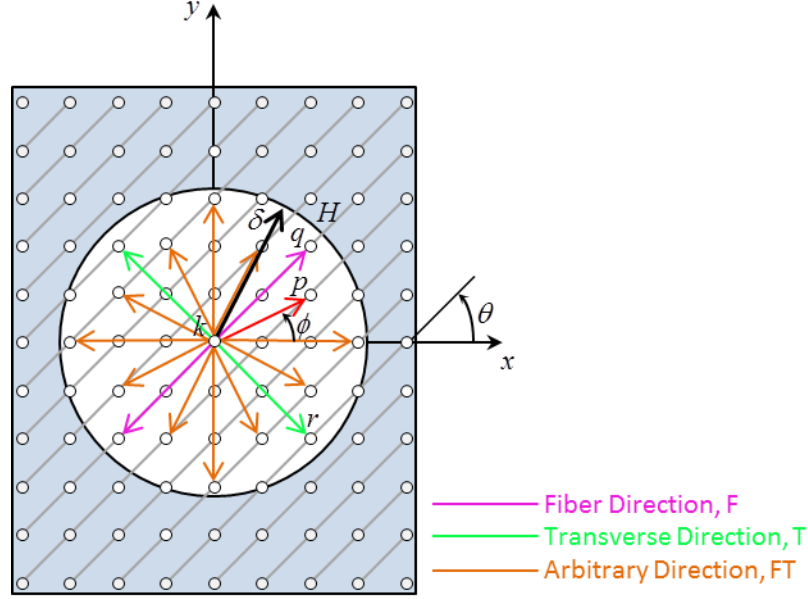


**Figure 2.** PD horizon for a family of material points and their interactions in a lamina.

As derived by Madenci and Oterkus (2013), the equation of motion for material point  $\mathbf{x}_{(k)}^n$  located on the  $n^{th}$  layer of a laminate with  $N$  layers can be expressed as

$$\begin{aligned} \rho_{(k)}^n \ddot{\mathbf{u}}_{(k)}^n = & \sum_{j=1} \left[ \mathbf{t}_{(k)(j)}^n \left( \mathbf{u}_{(j)}^n - \mathbf{u}_{(k)}^n, \mathbf{x}_{(j)}^n - \mathbf{x}_{(k)}^n, t \right) - \mathbf{t}_{(j)(k)}^n \left( \mathbf{u}_{(k)}^n - \mathbf{u}_{(j)}^n, \mathbf{x}_{(k)}^n - \mathbf{x}_{(j)}^n, t \right) \right] V_{(j)}^n \\ & + \sum_{m=n+1, n-1} \mathbf{p}_{(k)}^{(n)(m)} V_{(k)}^m + 2 \sum_{m=n+1, n-1} \sum_{j=1} \mathbf{q}_{(k)(j)}^{(n)(m)} V_{(j)}^m + \mathbf{b}_{(k)}^n \end{aligned} \quad (6)$$

where the material point,  $\mathbf{x}_{(k)}^n$  on the  $n^{th}$  layer is associated with an incremental volume,  $V_{(k)}^n$  and a mass density of  $\rho_{(k)}^n$ ;  $t$  designates time. With respect to a Cartesian coordinate system, the material point,  $\mathbf{x}_{(k)}^n$  experiences displacement,  $\mathbf{u}_{(k)}^n$ , and its location is described by the position vector,  $\mathbf{y}_{(k)}$  in the deformed state. The displacement and body load vectors at material point,  $\mathbf{x}_{(k)}^n$ , are represented by  $\mathbf{u}_{(k)}^n$  and  $\mathbf{b}_{(k)}^n$ , respectively. The motion of a material point conforms to the Lagrangian description of motion.

Arising from in-plane deformation,  $\mathbf{t}_{(k)(j)}^n$  represents the force density that material point,  $\mathbf{x}_{(j)}^n$  exerts up on material point,  $\mathbf{x}_{(k)}^n$ . The force density-stretch relationships can be expressed as

$$\mathbf{t}_{(k)(j)}^n(\mathbf{u}_{(j)} - \mathbf{u}_{(k)}, \mathbf{x}_{(j)} - \mathbf{x}_{(k)}, t) = \frac{1}{2} A_{(k)(j)} \frac{\mathbf{y}_{(j)} - \mathbf{y}_{(k)}}{|\mathbf{y}_{(j)} - \mathbf{y}_{(k)}|} \quad (7)$$

and

$$\mathbf{t}_{(j)(k)}^n(\mathbf{u}_{(k)} - \mathbf{u}_{(j)}, \mathbf{x}_{(k)} - \mathbf{x}_{(j)}, t) = -\frac{1}{2} B_{(j)(k)} \frac{\mathbf{y}_{(k)} - \mathbf{y}_{(j)}}{|\mathbf{y}_{(k)} - \mathbf{y}_{(j)}|} \quad (8)$$

where  $A_{(k)(j)}$  and  $B_{(j)(k)}$  are auxiliary parameters. The PD strain energy density at point  $\mathbf{x}_{(k)}$  for in-plane deformations can be expressed as

$$\begin{aligned} W_{(k)} = & a \theta_{(k)}^2 + b_F \sum_{j=1}^J \frac{\delta}{|\mathbf{x}_{(j)} - \mathbf{x}_{(k)}|} \left( |\mathbf{y}_{(j)} - \mathbf{y}_{(k)}| - |\mathbf{x}_{(j)} - \mathbf{x}_{(k)}| \right)^2 V_{(j)} \\ & + b_{FT} \sum_{j=1}^{\infty} \frac{\delta}{|\mathbf{x}_{(j)} - \mathbf{x}_{(k)}|} \left( |\mathbf{y}_{(j)} - \mathbf{y}_{(k)}| - |\mathbf{x}_{(j)} - \mathbf{x}_{(k)}| \right)^2 V_{(j)} \\ & + b_T \sum_{j=1}^J \frac{\delta}{|\mathbf{x}_{(j)} - \mathbf{x}_{(k)}|} \left( |\mathbf{y}_{(j)} - \mathbf{y}_{(k)}| - |\mathbf{x}_{(j)} - \mathbf{x}_{(k)}| \right)^2 V_{(j)} \end{aligned} \quad (9)$$

in which the PD parameter  $a$  is associated with the deformation associated with the dilatation,  $\theta_{(k)}$ , of the matrix. The remaining PD parameters,  $b_F$ ,  $b_T$ , and  $b_{FT}$ , are associated with deformation of material points in the fiber, transverse, and arbitrary directions, respectively. The fiber and transverse interactions exists only in the directions parallel and transverse to the fiber, and therefore, are limited to  $j=1, J$ . The arbitrary interactions exist in all directions. The PD dilation,  $\theta_{(k)}$ , of the matrix can be expressed as

$$\theta_{(k)} = d \sum_{j=1}^{\infty} \frac{\delta}{|\mathbf{x}_{(j)} - \mathbf{x}_{(k)}|} \left( |\mathbf{y}_{(j)} - \mathbf{y}_{(k)}| - |\mathbf{x}_{(j)} - \mathbf{x}_{(k)}| \right) \Lambda_{(k)(j)} V_{(j)} \quad (10)$$

The auxiliary parameters,  $A_{(k)(j)}$  and  $B_{(j)(k)}$ , can be determined using the relationship between force density vector and the strain energy density,  $W_{(k)}$ , at material point  $k$ , which is expressed in the form

$$\mathbf{t}_{(k)(j)}(\mathbf{u}_{(j)} - \mathbf{u}_{(k)}, \mathbf{x}_{(j)} - \mathbf{x}_{(k)}, t) = \frac{1}{V_{(j)}} \frac{\partial W_{(k)}}{\partial (|\mathbf{y}_{(j)} - \mathbf{y}_{(k)}|)} \frac{\mathbf{y}_{(j)} - \mathbf{y}_{(k)}}{|\mathbf{y}_{(j)} - \mathbf{y}_{(k)}|} \quad (11)$$

Following the substitution and performing the differentiation, the auxiliary parameters,  $A_{(k)(j)}$  and  $B_{(j)(k)}$ , can be expressed in terms of the PD material parameters as

$$A_{(k)(j)} = 4ad \frac{\delta}{|\mathbf{x}_{(j)} - \mathbf{x}_{(k)}|} \Lambda_{(k)(j)} \theta_{(k)} + 4\delta (\mu_F b_F + b_{FT} + \mu_T b_T) s_{(k)(j)}, \quad (12a)$$

and

$$B_{(j)(k)} = 4ad \frac{\delta}{|\mathbf{x}_{(k)} - \mathbf{x}_{(j)}|} \Lambda_{(j)(k)} \theta_{(j)} + 4\delta (\mu_F b_F + b_{FT} + \mu_T b_T) s_{(j)(k)} \quad (12b)$$

with

$$s_{(k)(j)}^{(n)} = \frac{|\mathbf{y}_{(j)}^n - \mathbf{y}_{(k)}^n| - |\mathbf{x}_{(j)}^n - \mathbf{x}_{(k)}^n|}{|\mathbf{x}_{(j)}^n - \mathbf{x}_{(k)}^n|} \quad (13a)$$

and

$$\mu_F = \begin{cases} 1 & (\mathbf{x}_{(j)} - \mathbf{x}_{(k)}) // \text{fiber direction} \\ 0 & \text{otherwise} \end{cases} \quad (13b)$$

and

$$\mu_T = \begin{cases} 1 & (\mathbf{x}_{(j)} - \mathbf{x}_{(k)}) \perp \text{fiber direction} \\ 0 & \text{otherwise} . \end{cases} \quad (13c)$$

The force density vectors,  $\mathbf{p}_{(k)}^{(n)(m)}$  and  $\mathbf{q}_{(k)(j)}^{(n)(m)}$  with  $m = (n+1), (n-1)$  develop due to the transverse normal and transverse shear deformations, respectively, between the material points  $\mathbf{x}_{(k)}^n$  and  $\mathbf{x}_{(k)}^m$ . The force density-stretch relationships can be expressed as

$$\mathbf{p}_{(k)}^{(n)(m)} = C_{(k)}^{(n)(m)} \frac{\mathbf{y}_{(k)}^m - \mathbf{y}_{(k)}^n}{|\mathbf{y}_{(k)}^m - \mathbf{y}_{(k)}^n|}, \quad (14a)$$

and

$$\mathbf{q}_{(k)(j)}^{(n)(m)} = D_{(k)(j)}^{(n)(m)} \frac{\mathbf{y}_{(j)}^m - \mathbf{y}_{(k)}^n}{|\mathbf{y}_{(j)}^m - \mathbf{y}_{(k)}^n|}, \quad (14b)$$

where  $C_{(k)}^{(n)(m)}$ , and  $D_{(k)(j)}^{(n)(m)}$  are auxiliary parameters. Within a composite laminate, there commonly exists a resin rich matrix region between lamina that behaves as an isotropic linear elastic material. Therefore the strain energy expression will be consistent with this form. The explicit form of the strain energy density functions,  $\hat{W}_{(k)}^n$  and  $\tilde{W}_{(k)}^n$ , for transverse normal and transverse shear deformations can be written as

$$\hat{W}_{(k)}^n = b_N \sum_{m=n+1, n-1} \frac{\hat{\delta}}{|\mathbf{x}_{(k)}^m - \mathbf{x}_{(k)}^n|} \left( |\mathbf{y}_{(k)}^m - \mathbf{y}_{(k)}^n| - |\mathbf{x}_{(k)}^m - \mathbf{x}_{(k)}^n| \right)^2 V_{(k)}^m \quad (15a)$$

and

$$\begin{aligned} \tilde{W}_{(k)}^n = b_S \sum_{m=n+1, n-1} \sum_{j=1}^{\infty} \frac{\tilde{\delta}}{|\mathbf{x}_{(j)}^m - \mathbf{x}_{(k)}^n|} & \left[ \left( |\mathbf{y}_{(j)}^m - \mathbf{y}_{(k)}^n| - |\mathbf{x}_{(j)}^m - \mathbf{x}_{(k)}^n| \right) \right. \\ & \left. - \left( |\mathbf{y}_{(k)}^m - \mathbf{y}_{(j)}^n| - |\mathbf{x}_{(k)}^m - \mathbf{x}_{(j)}^n| \right) \right]^2 V_{(j)}^m, \end{aligned} \quad (15b)$$

in which the PD parameters  $b_N$  and  $b_S$  are associated with the transverse normal and transverse shear deformations, respectively, existing between bonded lamina. The parameter  $\hat{\delta}$  is the horizon size in the thickness direction and  $\tilde{\delta}$  is defined as

$$\tilde{\delta} = \sqrt{\delta^2 + \hat{\delta}^2}.$$

The auxiliary parameters,  $C_{(k)}^{(n)(m)}$ , and  $D_{(k)(j)}^{(n)(m)}$ , can be determined using the relationship between force density vector and the strain energy density,  $\hat{W}_{(k)}^n$  and  $\tilde{W}_{(k)}^n$ , at material point  $k$ , which are expressed in the form (Madenci and Oterkus, 2013)

$$\mathbf{p}_{(k)}^{(n)(m)} = \frac{2}{V_{(k)}^m} \frac{\partial \hat{W}_{(k)}^n}{\partial \left( \left| \mathbf{y}_{(k)}^m - \mathbf{y}_{(k)}^n \right| \right)} \frac{\mathbf{y}_{(k)}^m - \mathbf{y}_{(k)}^n}{\left| \mathbf{y}_{(k)}^m - \mathbf{y}_{(k)}^n \right|}, \quad (16a)$$

and

$$\mathbf{q}_{(k)(j)}^{(n)(m)} = \frac{2}{V_{(j)}^m} \frac{\partial \tilde{W}_{(k)}^n}{\partial \left( \left| \mathbf{y}_{(j)}^m - \mathbf{y}_{(k)}^n \right| \right)} \frac{\mathbf{y}_{(j)}^m - \mathbf{y}_{(k)}^n}{\left| \mathbf{y}_{(j)}^m - \mathbf{y}_{(k)}^n \right|}, \quad (16b)$$

Following the substitution and performing the differentiation, the auxiliary parameters,  $C_{(k)}^{(n)(m)}$ , and  $D_{(k)(j)}^{(n)(m)}$  can be expressed in terms of the PD material parameters as

$$\mathbf{p}_{(k)}^{(n)(m)} = 4b_N \left( \left| \mathbf{y}_{(k)}^m - \mathbf{y}_{(k)}^n \right| - \left| \mathbf{x}_{(k)}^m - \mathbf{x}_{(k)}^n \right| \right) \frac{\mathbf{y}_{(k)}^m - \mathbf{y}_{(k)}^n}{\left| \mathbf{y}_{(k)}^m - \mathbf{y}_{(k)}^n \right|} \quad (17a)$$

and

$$\mathbf{q}_{(k)(j)}^{(n)(m)} = 4b_S \left[ \left( \left| \mathbf{y}_{(j)}^m - \mathbf{y}_{(k)}^n \right| - \left| \mathbf{x}_{(j)}^m - \mathbf{x}_{(k)}^n \right| \right) - \left( \left| \mathbf{y}_{(k)}^m - \mathbf{y}_{(j)}^n \right| - \left| \mathbf{x}_{(k)}^m - \mathbf{x}_{(j)}^n \right| \right) \right] \frac{\mathbf{y}_{(j)}^m - \mathbf{y}_{(k)}^n}{\left| \mathbf{y}_{(j)}^m - \mathbf{y}_{(k)}^n \right|} \quad (17b)$$

### 3.1 Material parameters

The PD material parameters can be obtained in terms of engineering material constants by considering simple loading conditions and equating the PD strain energy density to the strain energy density from the classical continuum mechanics. The PD material parameters,  $a$ ,  $d$ ,  $b_F$ ,  $b_T$ , and  $b_{FT}$ , related to in-plane deformations can be obtained by considering four different loading conditions: simple shear, uniaxial stretch in fiber direction, uniaxial stretch in transverse direction, and biaxial stretch. The PD material parameters,  $b_N$  and  $b_S$ , associated with transverse deformations can be obtained by considering two different loading conditions: transverse normal stretch and simple transverse shear.

As derived by Madenci and Oterkus (2013), the parameters can be related to the four independent material constants of elastic modulus in the fiber direction,  $E_{11}$ , elastic modulus in the transverse direction,  $E_{22}$ , in-plane shear modulus,  $G_{12}$ , and in-plane Poisson's ratio,  $\nu_{12}$  as

$$a = \frac{1}{2}(Q_{12} - Q_{66}) \quad (18a)$$

$$d = \frac{2}{\pi h \delta^3} \quad (18b)$$

$$b_F = \frac{(Q_{11} - Q_{12} - 2Q_{66})}{2\delta \left( \sum_{j=1}^J |\mathbf{x}_{(j)}^n - \mathbf{x}_{(k)}^n| V_{(j)} \right)}, \quad (18c)$$

$$b_T = \frac{(Q_{22} - Q_{12} - 2Q_{66})}{2\delta \left( \sum_{j=1}^N |\mathbf{x}_{(j)}^n - \mathbf{x}_{(k)}^n| V_{(j)} \right)}, \quad (18d)$$

$$b_{FT} = \frac{6Q_{66}}{\pi h \delta^4}, \quad (18e)$$

$$b_N = \frac{E_m}{\hat{\delta} \left[ (h_{n+1} + h_n) V_{(k)}^{n+1} + (h_{n-1} + h_n) V_{(k)}^{n-1} \right]}, \quad (18f)$$

$$b_S = \frac{G_m}{8\pi\tilde{\delta} \left( \left( \frac{h_{n+1} + h_n}{2} \right)^3 \left( \frac{\delta^2 + 2 \left( \frac{h_{n+1} + h_n}{2} \right)^2}{\sqrt{\delta^2 + \left( \frac{h_{n+1} + h_n}{2} \right)^2}} - (h_{n+1} + h_n) \right) + \left( \frac{h_{n-1} + h_n}{2} \right)^3 \left( \frac{\delta^2 + 2 \left( \frac{h_{n-1} + h_n}{2} \right)^2}{\sqrt{\delta^2 + \left( \frac{h_{n-1} + h_n}{2} \right)^2}} - (h_{n-1} + h_n) \right) \right)}, \quad (18g)$$

where

$$Q_{11} = \frac{E_{11}}{1 - \nu_{12}\nu_{21}}, \quad Q_{12} = \frac{\nu_{12}E_{22}}{1 - \nu_{12}\nu_{21}}, \quad Q_{22} = \frac{E_{22}}{1 - \nu_{12}\nu_{21}}, \quad Q_{66} = G_{12} \quad (19a)$$

$$S_{11} = \frac{1}{E_{11}}, \quad S_{12} = -\frac{\nu_{12}}{E_{11}} = -\frac{\nu_{21}}{E_{22}}, \quad S_{22} = \frac{1}{E_{22}}, \quad S_{66} = \frac{1}{G_{12}}. \quad (19b)$$

with  $\nu_{12}/E_{11} = \nu_{21}/E_{22}$  and  $E_m$  and  $G_m$  represent the Young's modulus and shear modulus of the matrix material. The resulting PD model of a laminate consists of laminae connected with transverse normal and shear deformations, and it accurately models the behavior of fiber reinforced laminate composites.

The PD material parameters are derived under the assumption that the material point located at  $\mathbf{x}$  is in a single material with its complete neighborhood entirely embedded within its horizon,  $\delta$ . However, this assumption becomes invalid when the material point is close to free surfaces or material interfaces. Therefore, there is a reduction in material stiffness near the free surfaces. On the other hand, stiffness near the interface can exhibit an increase or reduction, depending upon how dissimilar material regions interact across their interface. Since free surfaces and material interfaces vary from one problem to another, it is impractical to resolve this issue analytically. Therefore, the stiffness reduction or increase due to surfaces is corrected numerically. A surface and interface correction factors, as explained by Madenci and Oterkus (2013), can be used to account for the loss in stiffness near the surface and to accommodate the transition between dissimilar laminae.

A numerical treatment is necessary to solve for the PD equations of motion which involves differentiation with respect to time and spatial integration. The numerical treatment of the equations of motion, Eq. (6), involves the discretization of the domain of interest into subdomains. Within these subdomains, the velocity and displacement fields are assumed to be constant. Each subdomain can then be represented by a single collocation point located at the center of each subdomain. The details of the numerical treatment is also explained by Madenci and Oterkus (2013).

Solution of the PD equation of motion requires initial velocity and displacement conditions as well as boundary conditions. The introduction of displacement, velocity, or body force boundary conditions is different than the approach used in classical continuum mechanics due to the non-local nature of PD. The details of the introduction of the boundary conditions are discussed by Madenci and Oterkus (2013). The regions surrounding the boundary conditions require special treatment to prevent unrealistic damage accumulation. No fail regions are introduced in the region surrounding the boundary conditions to prevent this phenomenon.

Time integration of Eq. (6) is computationally expensive due to the small time-step size required for stable integration. This study concerns quasi-static loading; therefore, the adaptive dynamic relaxation (ADR) method, first utilized by Kilic and Madenci (2010), is used to solve the system of ordinary differential equations resulting from Eq. (6).

### **3.2. Numerical verification**

The response of fiber-reinforced composite laminate to loading is dependent on the material properties of each lamina, the lamina thicknesses, and the specific layup. The validity of the PDLT for composite laminates is demonstrated through comparisons with classical laminate theory (CLT) and FEM analysis by considering laminates with complex layup under in-plane tension and transverse pressure.



### 3.2.1 Laminates subjected to tensile loading

A four ply laminate subjected to uniaxial tensile loading is considered to demonstrate the capability of PDLT to capture the deformation of a laminate. The material system is fiberglass epoxy lamina. The material properties of the lamina are  $E_{11} = 38.6$  GPa,  $E_{22} = 10.3$  GPa,  $G_{12} = 4.5$  GPa, and  $\nu_{12} = 0.33$ . The length and width of each specimen is  $L = 1.6$  m and  $W = 1.0$  m, respectively. The grid size in the model is  $\Delta x = 0.01$  mm resulting in 160 points in the length direction and 100 material points in the width direction. The nominal ply thickness is  $t_k = 0.01$  m resulting in a total laminate thickness of  $h = 0.04$  m. The horizon is specified as  $\delta = 3.015\Delta x$ . The uniaxial tension is applied as a body load, equivalent to a stress resultant of  $N_x = 1000$  N/m, to the material points in a volumetric region at both ends of the plate extending the width of the laminate and a length of  $b = 0.1$  m. During the solution, failure is not allowed and the analysis is run until the system reaches equilibrium. Four separate layups are considered to demonstrate the ability of the PD formulation to capture the behavior of a laminated composite.

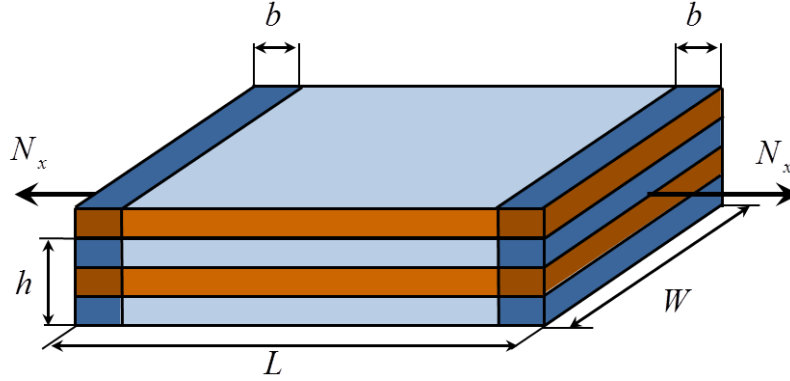


**Figure 3.** Geometry of a composite laminate under uniaxial tensile loading

The first case is a symmetric cross-ply laminate with a layup of  $[0^\circ/90^\circ]_s$ . For symmetric laminates, CLT predicts that there is no coupling between bending and extension. Therefore, the panel exhibits only in-plane deformations for the prescribed loading condition. Displacement contours on the mid-plane of the laminate are shown in Fig. 4. The variations of the in-plane displacement components at the mid-line of the laminate are compared with the analytical results from the CLT in Figs. 5 and 6.

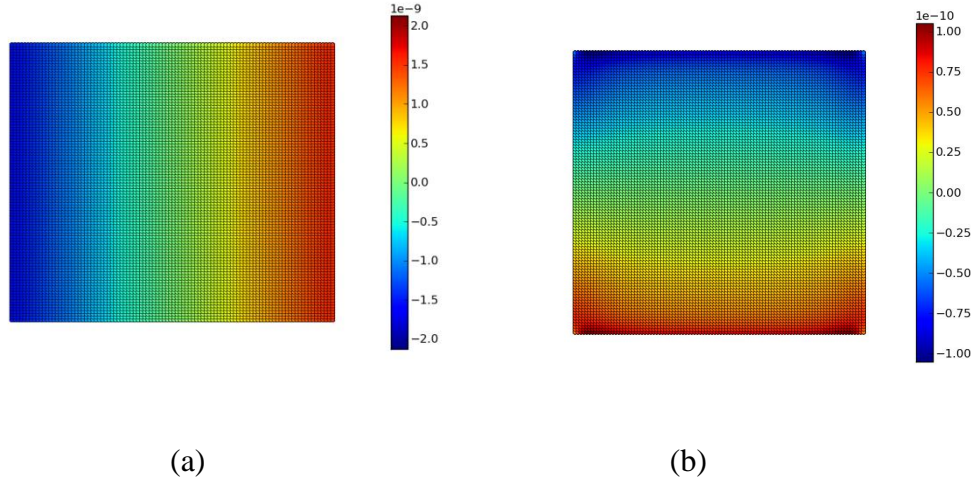


**Figure 4.** Displacement contours for the  $[0^\circ / 90^\circ]_5$  laminate subjected to an uniaxial tensile load: a) ( $u_x$ ) and b) ( $u_y$ )

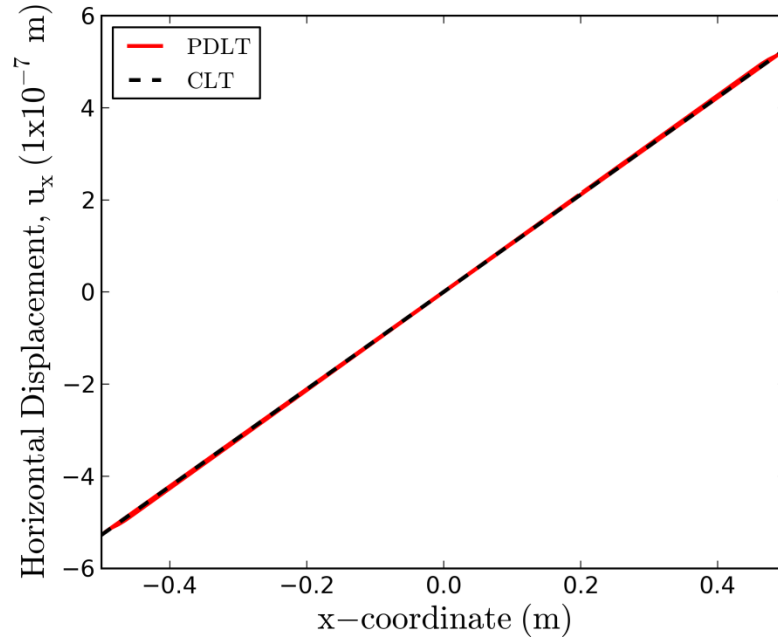


**Figure 5.** Horizontal displacement ( $u_x$ ) along the central axis for the  $[0^\circ / 90^\circ]_5$  laminate.

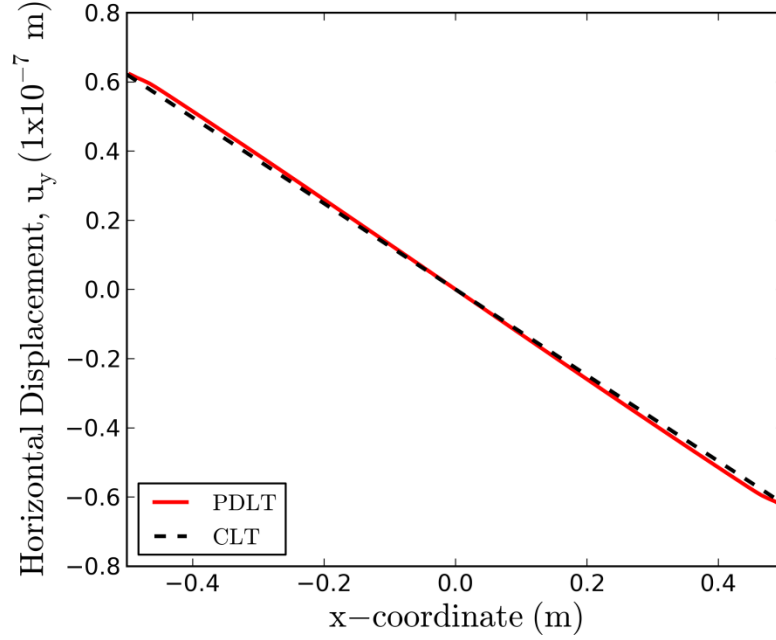


**Figure 6** Horizontal displacement ( $u_y$ ) perpendicular to the central axis for the  $[0^\circ / 90^\circ]_s$  laminate

The next case considers a unidirectional  $[45^\circ]_4$  angle ply laminate with the fibers oriented in the off-axis direction to induce a stretching-shearing coupling behavior when subjected to the prescribed loading condition. Figure 7 shows the stretching-shearing coupling behavior in the plane of the laminate. The variations of the in-plane displacement components at the mid-line of the laminate are compared with the analytical results from the CLT in Figs. 8 and 9.

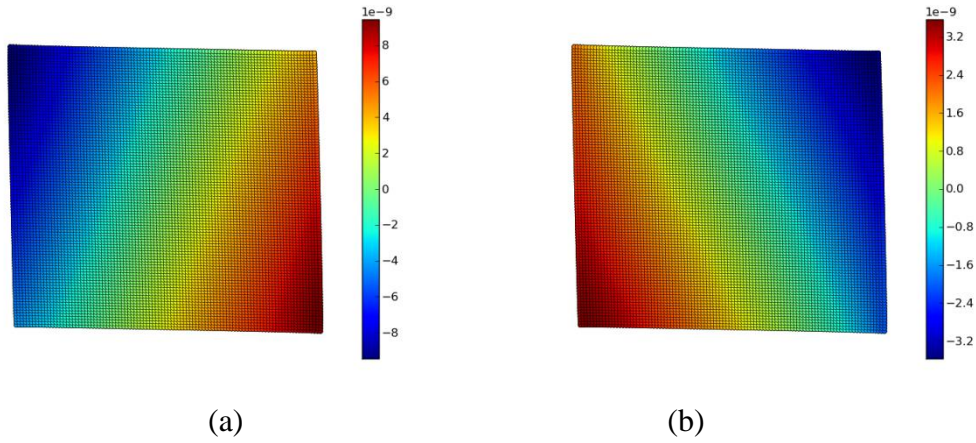


**Figure 7** Displacement contours for the  $[45^\circ]_4$  laminate subjected to a uniaxial tensile load: a) ( $u_x$ ) and b) ( $u_y$ )

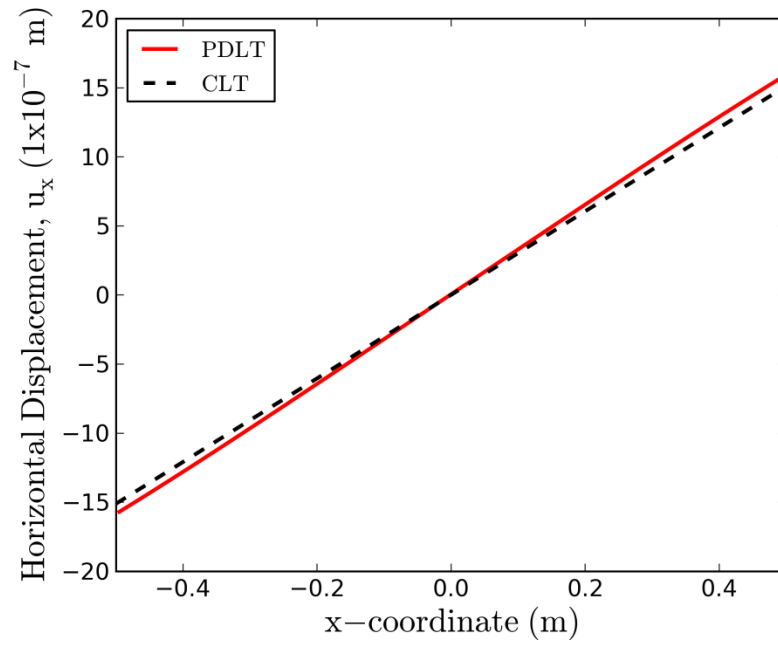


**Figure 8** Horizontal displacement ( $u_x$ ) along the central axis for the  $[45^\circ]_4$  laminate.

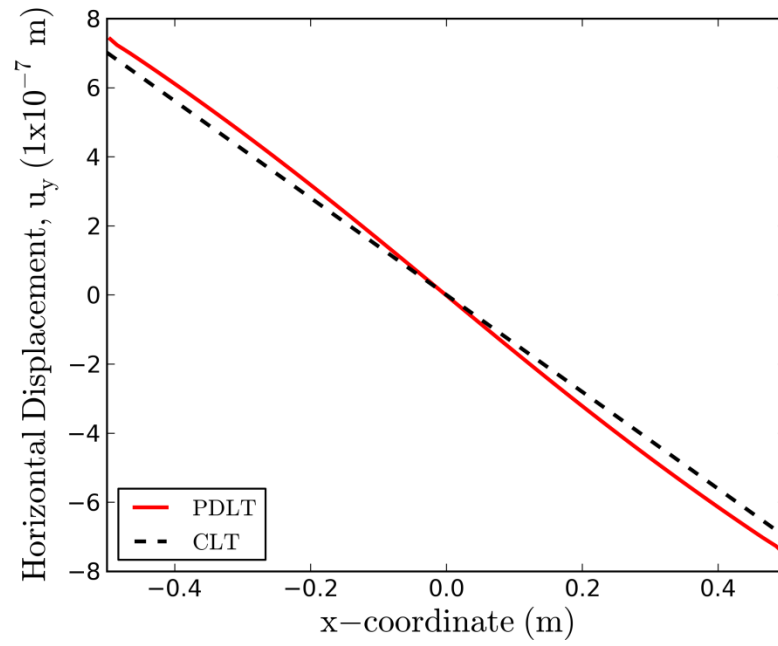


**Figure 9** Horizontal displacement ( $u_y$ ) perpendicular to the central axis for the  $[45^\circ]_4$  laminate.

The third case considers an anti-symmetric  $[-45^\circ / -45^\circ / 45^\circ / 45^\circ]$  laminate. When subjected to the prescribed uniaxial tensile loading, it experiences stretching-twisting interaction as shown in Fig. 10. The variations of all the displacement components at the mid-line of the laminate are compared with the analytical results from the CLT in Figs. 11, 12, and 13.

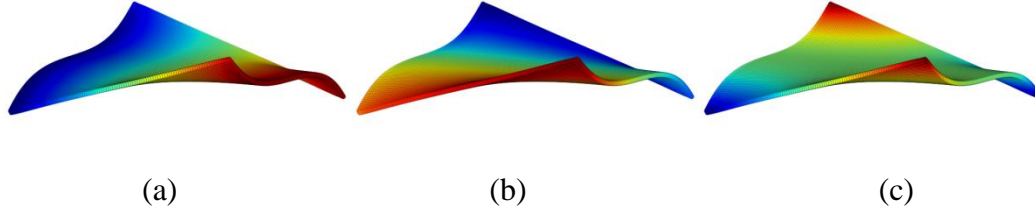


**Figure 10** Displacement contours for the  $[-45^\circ / -45^\circ / 45^\circ / 45^\circ]$  laminate subjected to an uniaxial tensile load: a)  $(u_x)$ , b)  $(u_y)$  and c)  $(u_z)$

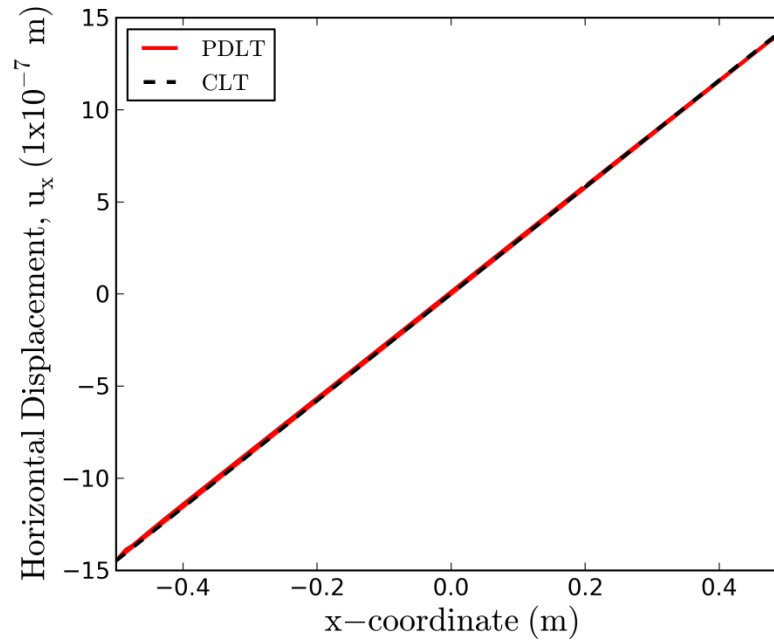


**Figure 11** Horizontal displacement  $(u_x)$  along the central axis for the  $[-45^\circ / -45^\circ / 45^\circ / 45^\circ]$  anti-symmetric laminate.

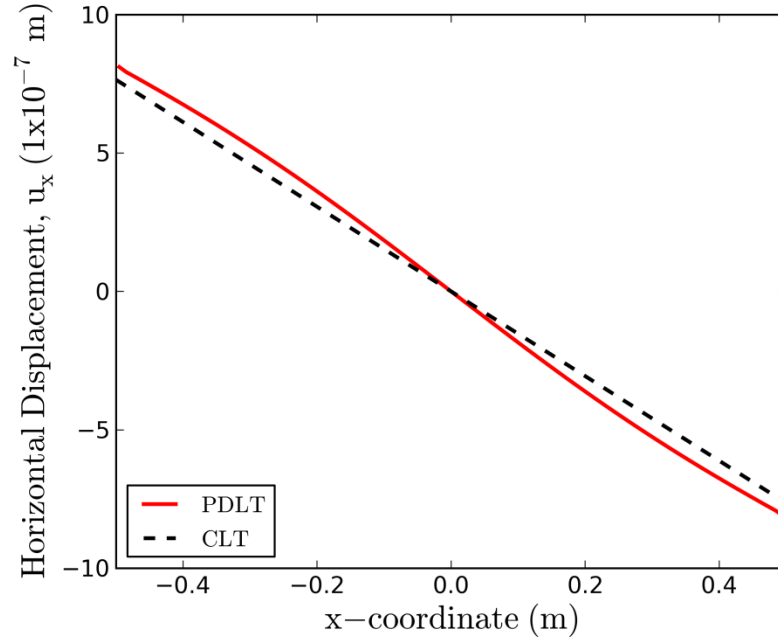


**Figure 12** Horizontal displacement ( $u_y$ ) perpendicular to the central axis for the  $[-45^\circ / -45^\circ / 45^\circ / 45^\circ]$  anti-symmetric laminate.

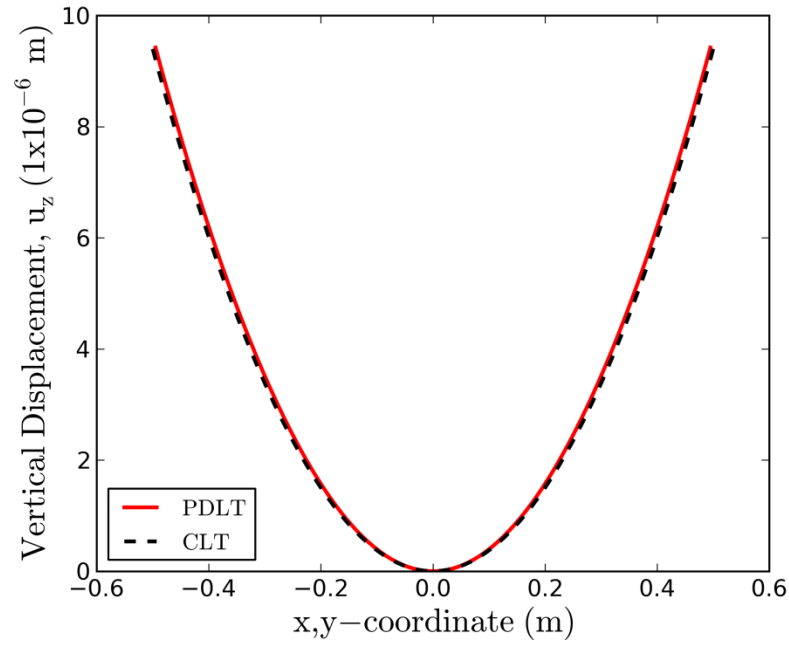


**Figure 13** Vertical displacement ( $u_z$ ) along the central axis for the  $[-45^\circ / -45^\circ / 45^\circ / 45^\circ]$  anti-symmetric laminate.

The final case considers a  $[0^\circ / 90^\circ / 0^\circ / 90^\circ]$  laminate, which exhibits stretching-bending deformations when subjected to the uniaxial tension as shown in Fig. 14. The variation of the displacement components at the mid-line of the laminate are compared with the analytical results from the CLT in Figs. 15, 16, and 17.

For all these complex laminate layups, the PD theory captures the expected deformation couplings, and there is a good agreement between the PD and analytical displacements.

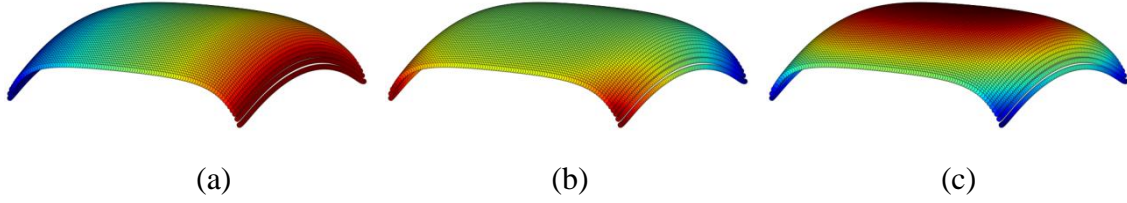


**Figure 14** Displacement contours for the  $[0^\circ / 90^\circ / 0^\circ / 90^\circ]$  laminate subjected to an uniaxial tensile load: a)  $(u_x)$ , b)  $(u_y)$  and c)  $(u_z)$

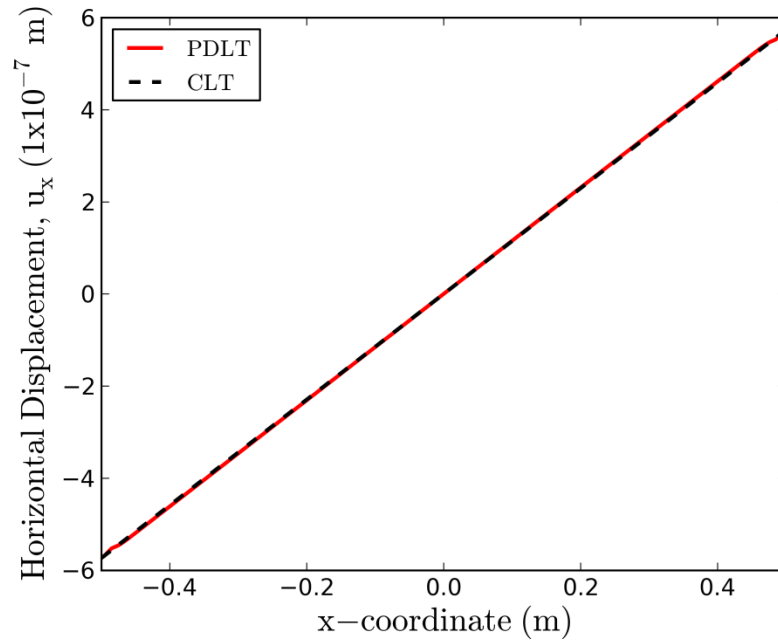


**Figure 15** Horizontal displacement  $(u_x)$  along the central axis for the  $[0^\circ / 90^\circ / 0^\circ / 90^\circ]$  laminate.

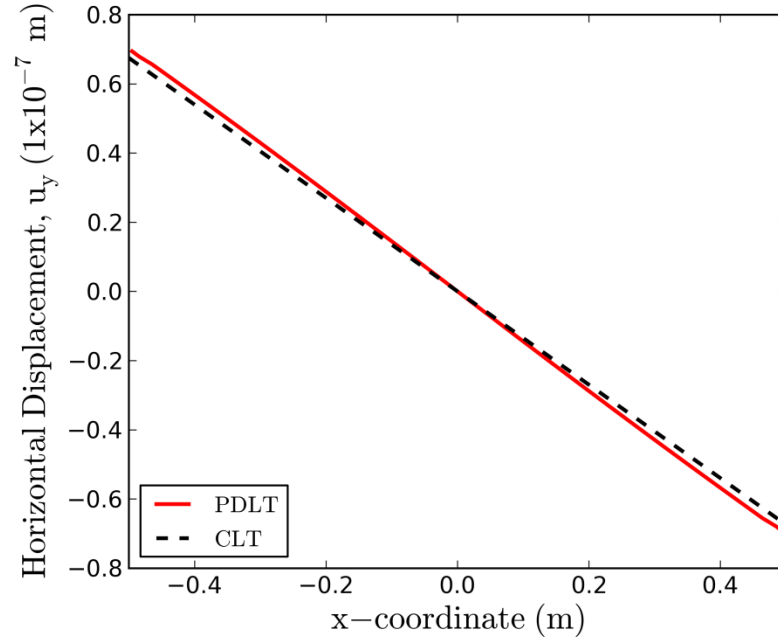


**Figure 16** Horizontal displacement ( $u_y$ ) perpendicular to the central axis for the  $[0^\circ / 90^\circ / 0^\circ / 90^\circ]$  laminate.

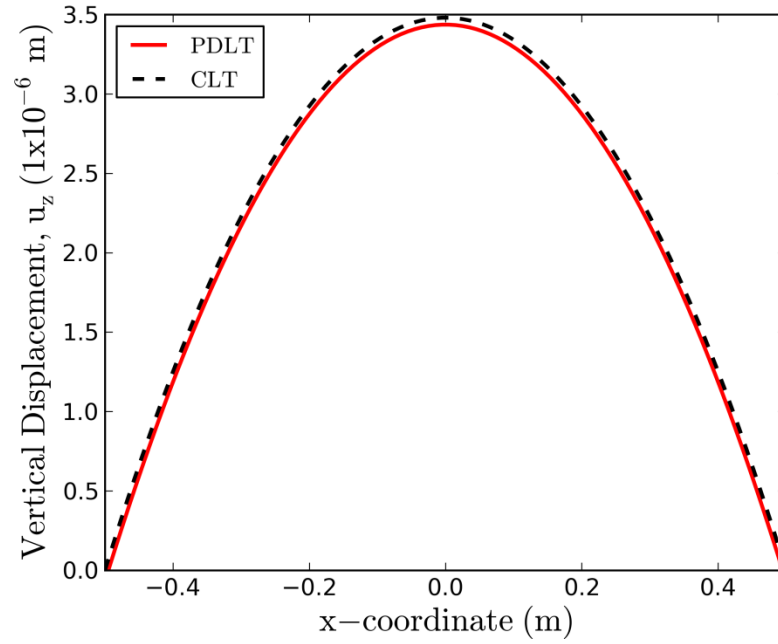


**Figure 17** Vertical displacement ( $u_z$ ) along the central axis for the  $[0^\circ / 90^\circ / 0^\circ / 90^\circ]$  laminate.



### 3.2.2 Laminate with a hole subjected to tensile loading

A laminate with a layup of  $[0^\circ / 45^\circ / 45^\circ / 0^\circ]$ , with a central hole, is subjected to uniaxial tensile loading to demonstrate the capability of PD laminate theory to accurately model complex laminates. The material system is unidirectional AS4/3501-6 carbon fiber epoxy lamina. The material properties of the lamina are  $E_{11} = 142$  GPa,  $E_{22} = 10.3$  GPa,  $G_{12} = 4.5$  GPa, and  $\nu_{12} = 0.27$ . The length and width of each specimen is  $L = 1.0$  m and  $W = 1.0$  m, respectively. The grid size in the model is  $\Delta x = 0.01$  mm resulting in 100 points in the length direction and 100 material points in the width direction. The nominal ply thickness is  $t_k = 0.01$  m resulting in a total laminate thickness of  $h = 0.04$  m. The horizon is specified as  $\delta = 3.015\Delta x$ . The uniaxial tension is applied as a body load, equivalent to a stress resultant of  $N_x = 4.26 \times 10^6$  N/m, to the material points in a volumetric region at both ends of the plate extending the width of the laminate and a length of  $b = 0.03$  m. During the solution, failure is not allowed and the analysis is run until the system reaches equilibrium.

Figure 18 shows the contour plots of the displacement components, and deformed shape. The variations of the  $u_x$  displacement in the  $x$  direction are obtained for each of the layers of the laminate along the mid-line as well as along the edge and compared with analytical results from the CLT in Figs. 19. There is a good agreement between the PD and analytical displacements away from the central hole. The PDLT clearly captures the coupling between in-plane shear and extension type deformations.

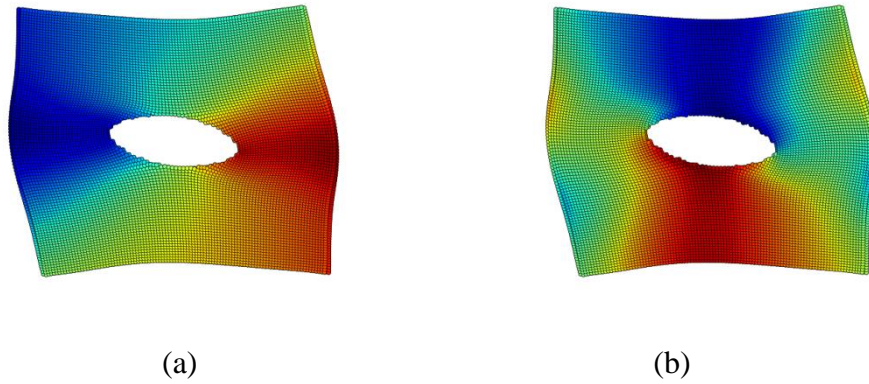


**Figure 18** Displacement contours for the  $[0^\circ / 45^\circ / 45^\circ / 0^\circ]$  laminate subjected to an uniaxial tensile load: a) ( $u_x$ ) and b) ( $u_y$ )

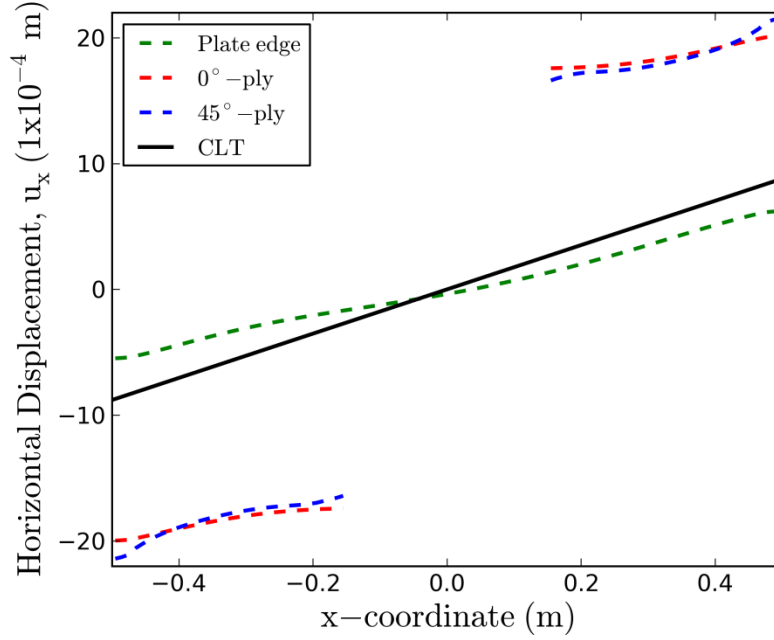


**Figure 19** Horizontal displacement ( $u_x$ ) for the  $[0^\circ / 45^\circ / 45^\circ / 0^\circ]$  laminate.

### 3.2.3 Laminate subjected to three point bending

A quasi-isotropic laminate with layup  $[0^\circ / 90^\circ / -45^\circ / 45^\circ]_s$  is subjected to three point bending to demonstrate the capability of PDLT in the presence of transverse loading as shown in Fig.20. The material system is unidirectional AS4/3501-6 carbon fiber epoxy lamina. The material properties of the lamina are  $E_{11} = 142$  GPa,  $E_{22} = 10.3$  GPa,  $G_{12} = 4.5$  GPa, and  $\nu_{12} = 0.27$ . The length and width of each specimen is  $L = .1025$  m and  $W = .025$  m, respectively. The grid size in the model is  $\Delta x = 0.0025$  mm resulting in 41 points in the length direction and 10 material points in the width direction. The nominal ply thickness is  $t_k = 0.00013$  m resulting in a total laminate thickness of  $h = 0.00104$  m. The horizon is specified as  $\delta = 3.015\Delta x$ . A displacement boundary condition of  $u_3 = 0$  was enforced on the material points residing on the third layer along the width at each end of the laminate. The central load is applied as a body load, equivalent to a pressure of  $P_z = 1000$  N/m<sup>2</sup>, to the material points in a volumetric region at the center the plate extending the width and thickness of the laminate along a length of  $b = 0.02$  m. During the solution, failure is not allowed, and the analysis is run until the system reaches equilibrium. The variations of the  $u_z$  displacements in the  $x$  direction and the  $z$  direction are obtained at the mid-plane of the laminate, and compared with the FEM results in Figs. 21-22. There is a good agreement between the PD predictions and those of Refined Zigzag Theory (RZT) element (Barut et al. 2013).

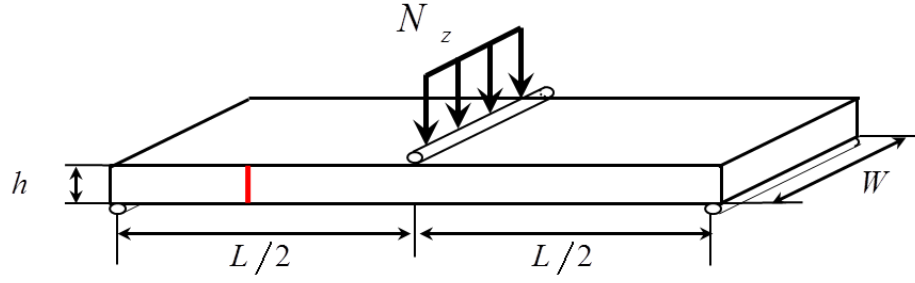


**Figure 20** Loading and geometry of a composite laminate under three point bending.

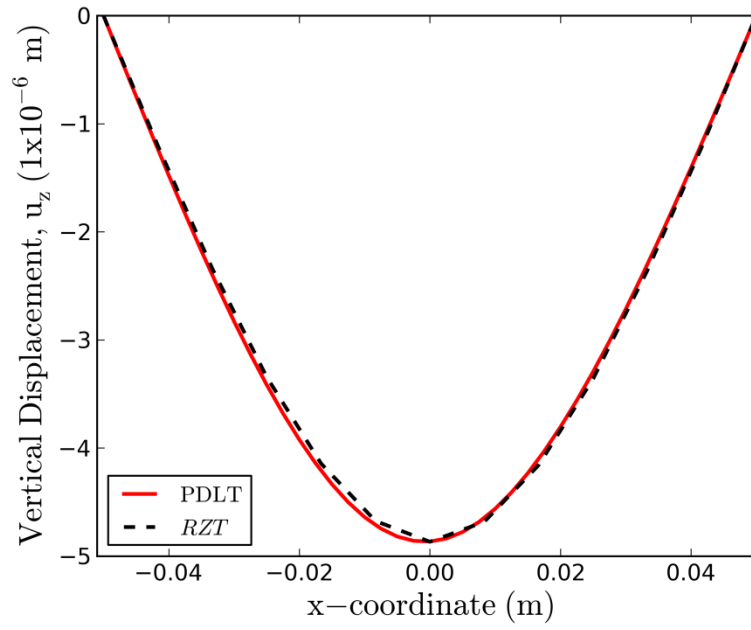


**Figure 21** Vertical displacement ( $u_z$ ) along the central axis for the  $[0^\circ / 90^\circ / -45^\circ / 45^\circ]_s$  laminate.

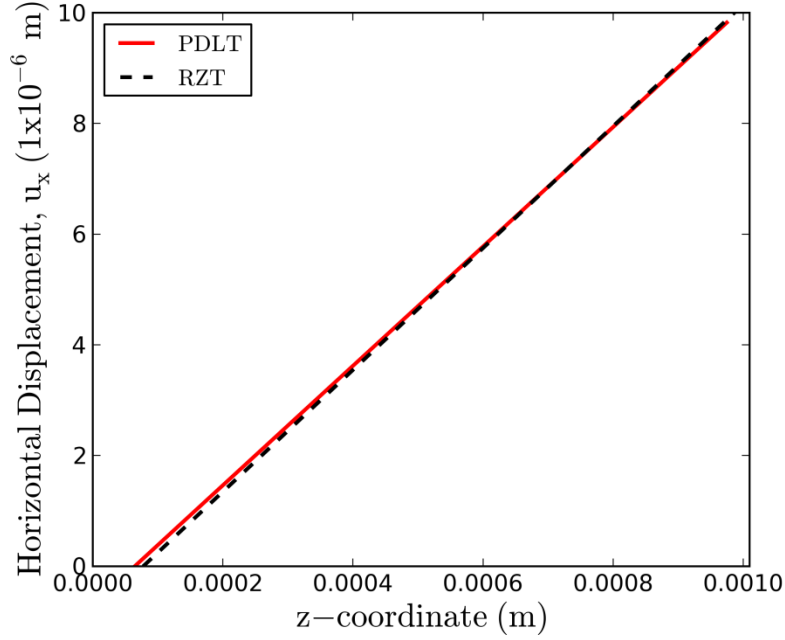


**Figure 22** Vertical displacement ( $u_z$ ) along the vertical axis of the  $[0^\circ / 90^\circ / -45^\circ / 45^\circ]_s$  laminate.

#### 4. Failure prediction

##### 4.1 Damage in monolithic material

Material damage in PD is introduced through elimination of interactions among the material points. It is assumed that when the stretch,  $s_{(k)(j)}$  between two material points  $k$  and  $j$  exceeds its critical value,  $s_c$  the onset of damage occurs. Based on the concept introduced by Silling and Askari (2005), the critical stretch for isotropic materials can be obtained as derived Madenci and Oterkus (2013) by relating the energy required to create a fracture surface in a material to the critical energy release rate of that material as

$$s_c = \begin{cases} \sqrt{\frac{G_c}{\left(3\mu + \left(\frac{3}{4}\right)^4 \left(\kappa - \frac{5\mu}{3}\right)\right) \delta}} & \text{3-D} \\ \sqrt{\frac{G_c}{\left(\frac{6}{\pi}\mu + \frac{16}{9\pi^2}(\kappa - 2\mu)\right) \delta}} & \text{2-D} \end{cases} \quad (20)$$

It is worth noting that the critical stretch is a function of the horizon. The value of the horizon brings in the effect of the physical material characteristics, nature of loading, length scale, and the computational cut-off radius. This simple relationship provides the

value of critical stretch for a linear elastic brittle material with a known critical energy release rate.

In order to include damage initiation in the material response, the force density vectors can be modified through a history-dependent scalar-valued function  $\mu$  (Silling and Bobaru, 2005). When the stretch between these material points exceeds its critical stretch, failure occurs; thus, the history-dependent scalar-valued function,  $\mu$  is zero rendering the associated part of the force density vector to be zero. Damage is reflected in the equations of motion by removing the force density vectors between the material points in an irreversible manner. As a result, the load is redistributed among the material points in the body, leading to a progressive damage growth in an autonomous fashion.

Local damage at a point is defined as the weighted ratio of the number of eliminated interactions to the total number of initial interactions of a material point with its family members. The local damage at a point can be quantified as (Silling and Askari, 2005)

$$\phi(\mathbf{x}, t) = 1 - \frac{\int_H \mu(\mathbf{x}' - \mathbf{x}, t) dV'}{\int_H dV'}. \quad (21)$$

The local damage ranges from zero to one. When the local damage is unity, all the interactions initially associated with the point are eliminated, while a local damage of zero means that all interactions are intact. The measure of local damage is an indicator of possible crack formation within a body. For example, initially a material point interacts with all materials in its horizon as shown in Fig. 23 (a); thus, the local damage has a value of 0. However, the creation of a crack terminates half of the interactions within its horizon resulting in a local damage value of  $\frac{1}{2}$ .

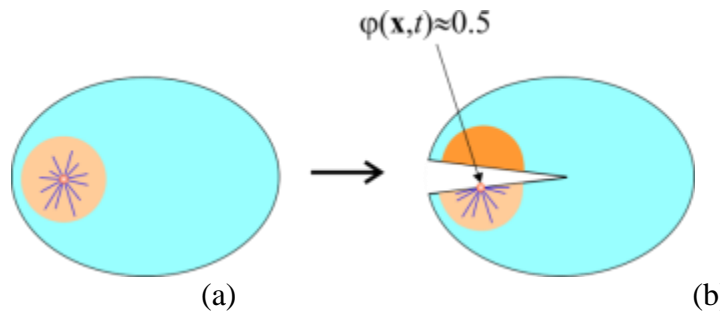


**Figure 23** (a) All interactions are intact (no damage), (b) Half of the terminated interactions create a crack.

At each time step in the numerical process, the displacement at each collocation point and the stretch between collocation points is computed. The stretch is monitored, and if it exceeds a critical value,  $s_c$ , then the interaction is terminated. The ratio of terminated interaction to total interactions at each collocation point is calculated during the numerical volume integration to obtain the local damage defined in Eq. (21).

A fracture surface can be defined as a region where no interactions between material points are present. Insertion of a crack in the PD model can be accomplished by breaking all the interactions across the surface of the crack. The insertion of a crack in this manner requires determining whether an interaction crosses the plane of a crack, which can be tedious depending on the location and orientation. If the interaction crosses the crack surface, then the interaction is terminated. Alternatively, a crack can be inserted by terminating the interaction if one of the material points is above the plane of the crack while the other is below the plane of the crack.

## 4.2 Damage in composite laminates

Five different interaction types are present in the PD formulation for fiber reinforced composite laminates to capture the major failure modes. This is accomplished by assigning unique critical stretch values to the different interaction types. The constitutive or force-stretch relations, for the interactions within the plane of a lamina, in the fiber, transverse, and arbitrary directions, are shown in Fig. 24. In this study, the transverse and arbitrary critical parameters are combined into a matrix critical stretch in tension and compression as  $s_{mt}$  and  $s_{mc}$ , respectively. The critical parameters in the fiber direction in tension and compression are  $s_{ft}$  and  $s_{fc}$ , respectively. The critical stretch parameters for composite laminates can be obtained using experimental methods (Oterkus et al., 2012), calibration using an inverse approach (Colavito et al., 2007a; 2007b) or through equating the energy required to create a fracture surface to the energy release rate (Hu et al., 2011, 2012).

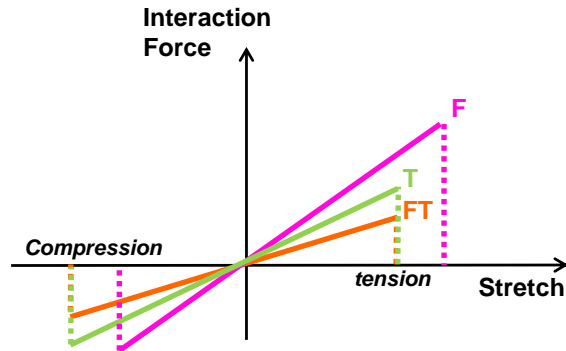


**Figure 24** Force-stretch relationships for peridynamic interactions

## 4.3 Inverse approach for critical stretch

The inverse approach is an alternative to the use of analytical critical stretch expression. This method combines the PD simulation with an experimental test to calibrate the critical stretch value. For the first step, a trial critical stretch is used in the PD simulation to obtain the peak failure load of the specimen. The PD prediction of the peak failure load is then compared to the experimentally observed peak failure load to determine if the trial critical stretch value is valid. If an unacceptable offset exists between the predicted and measured failure loads, then the trial critical stretch is adjusted with respect to the offset. The process is then repeated until the PD prediction of failure load is equal to the

experimental failure load. At the end of the iterative process, the critical stretch value is obtained.

#### 4.3.1 Monolithic materials

The applicability of the critical stretch as a failure parameter is demonstrated for a linear elastic material by considering the experimental study conducted by Ayatollahi and Aliha (2009). They considered diagonally loaded square plate specimens, shown in Fig. 25a, to investigate the effect of mode mixity ranging from pure mode I to pure mode II. They provided the failure loads, crack propagation paths for each of the specimens and fracture toughness of the material,  $K_{IC}$ . The edge length of the diagonal square is  $2W = 0.15$  m and its thickness is  $h = 0.005$  m. The length of the crack is  $2a = 0.045$  m with an orientation angle of  $\alpha$ . The material has an elastic modulus of  $E = 2940$  MPa, Poisson's ratio of  $\nu = 0.38$ , and fracture toughness of  $K_{IC} = 1.33 \text{ MPa}\sqrt{\text{m}}$ . They also reported the failure loads for varying crack orientation angles of  $\alpha = 0^\circ$  (Mode I),  $15^\circ$ ,  $30^\circ$ ,  $45^\circ$ ,  $62.5^\circ$  (Mode II). Center of the crack coincides with the origin of the Cartesian coordinate system. The applied load is introduced through a velocity constraint of  $V = 1 \times 10^{-9}$  m/s in the volume defined by dotted lines while enclosing the circular regions at opposite corners. The initial crack is inserted in the PD model by removing the interactions across the crack surface.

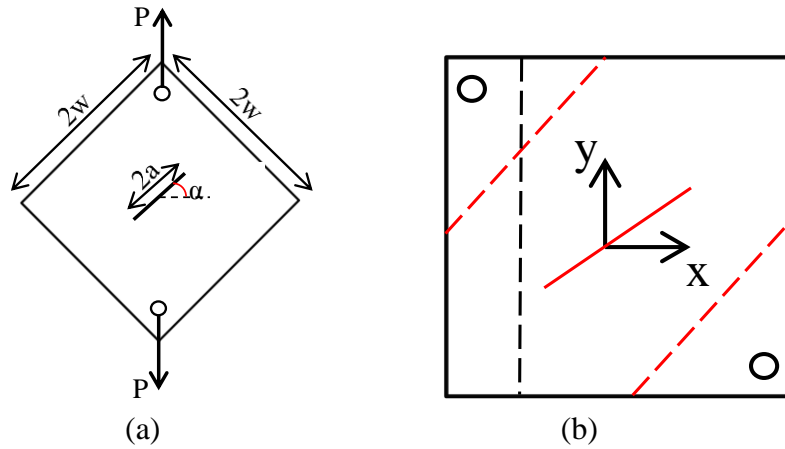


**Figure 25** a) DLSP Specimen b) PD model of DSPL.

The crack propagation paths obtained from the PD simulations and those of the experimental observations are plotted in Fig. 26. A good agreement is observed between the predictions and observed crack paths. Crack growth initiation angles are also compared between the predictions and measurements. Again, a very good comparison is obtained as shown in Fig. 27. Finally, the failure loads are compared, and it is observed that the failure loads obtained from the PD simulations are within 15% of the experimental values for all crack inclination angles as depicted in Fig. 28. While the PD simulations are close to the experimental results for pure Mode I case and pure Mode II cases, the mixed mode PD failure predictions are higher than the experimental values. A possible reason for this could be due to specimen preparation, which does not ensure a

sharp crack tip. The specimen preparation procedure requires the use of a fret saw to create a crack without additional cyclic loading. The inclined angle of the crack, coupled with the shape of the crack tip, could in effect change the cracks tip orientation causing the offset observed in the comparison. Despite this offset, the agreement is satisfactory; thus, validating the critical stretch value of 0.089.

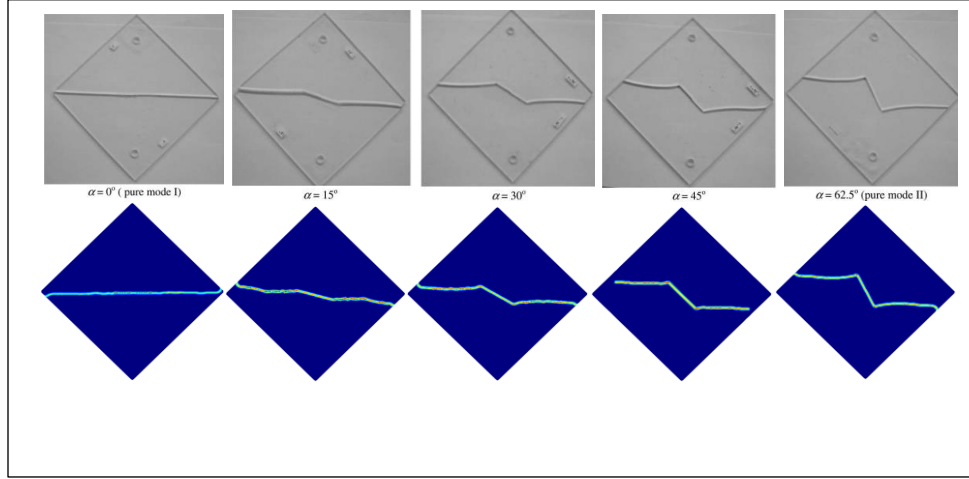


**Figure 26** Experimental and PD crack propagation paths

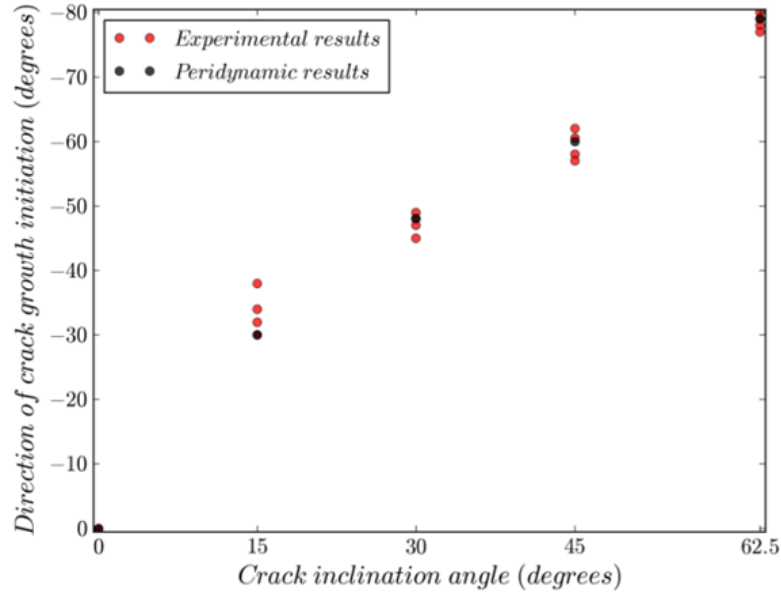


**Figure 27** Comparison of crack growth initiation angle between peridynamic and experimental results as a function of crack inclination angle.



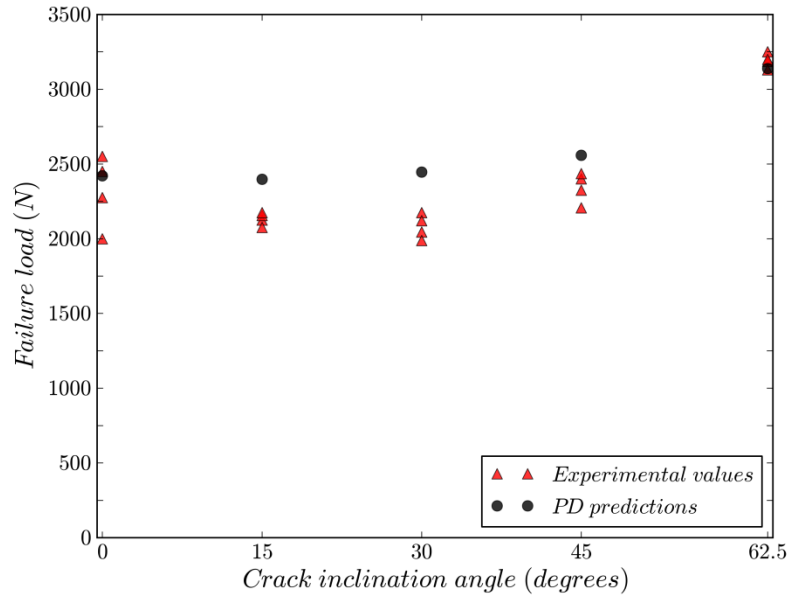


**Figure 28** Comparison of the failure load between peridynamic and experimental results as a function of crack inclination angle.

#### 4.3.2 Laminated composites

The inverse approach for monolithic materials is modified for the PDLT to accommodate the multiple interaction types and critical stretch values. To demonstrate the approach, the inverse method is used to obtain the fiber and matrix critical stretch values for a notched quasi-isotropic AS4/3501-6 laminates subjected to tensile and compressive loading. In the experimental study conducted by Wang et al. (2004), the tensile and compressive peak loads are obtained for a  $[45/0/-45/90]_{2S}$  panel with four different central hole diameters (2.00, 3.81, 6.35, and 9.55 mm). The following procedure is used to obtain the matrix and fiber critical stretch values for a horizon value of 0.0022914 m.

To utilize the inverse approach, several assumptions regarding the progression of failure are necessary. The first assumption is that the failure in tension depends primarily on matrix cracking. Therefore, the peak failure load of the laminate primarily depends on the tensile matrix critical stretch. This assumption is made after examination the failure patterns for two different laminates,  $[0/90]_{XS}$  and  $[45/-45]_{XS}$ . The failure modes present in the  $[0/90]_{XS}$  laminate are longitudinal fracture of the matrix in the  $90^\circ$  layer and fracture of the fibers in the  $0^\circ$  layer. The failure modes present in the  $[45/-45]_{XS}$  laminate are longitudinal fracture of the matrix for all layers and delamination between layers. For both laminates, the longitudinal fracture of the matrix precedes the other failure modes and dictates the final failure pattern, and allows for such an assumption. The second assumption concerning the laminate compressive strength is dictated by compressive fiber critical stretch. This assumption relies on the experimental observations of the progressive failure of the identical laminate specimen with a 6.35 mm

diameter hole. Suemasu et al. (2005) observed that damage first appeared due to fiber micro-buckling in the  $0^\circ$  layers. They also observed additional fiber micro-buckling in the  $0^\circ$  layers and inter-laminar delamination prior to a sudden failure of the laminate. Finally, the relationship between compressive and tensile critical stretch values is assumed to be equivalent to the ratio of the compressive and tensile strengths of the lamina. The longitudinal and compressive strength ratios are assumed to be equivalent to the fiber and matrix critical stretch ratios, respectively. The first two assumptions allow the tensile matrix and compressive fiber critical stretch values, while the third assumption allows the compressive matrix and tensile fiber critical stretch values to be obtained.

The laminate with the 6.35 mm central hole is used to calibrate the critical stretch values due to the additional experimental observations. In the first step, the tensile matrix critical stretch is calibrated using iterative PD simulations of the tensile loading of the notched laminate. The tensile matrix critical stretch is adjusted until the peak failure load for the PD simulation matches the measured value. For this step, the tensile fiber critical stretch is assigned an artificially high value to prevent failure due to fiber damage. Following this calibration, the tensile matrix critical stretch value is used to obtain the compressive matrix critical stretch value using the ratio of tensile to compressive transverse strength of the lamina,  $Y_t$  and  $Y_c$ , respectfully. The compressive matrix critical stretch is obtained by multiplying the strength ratio ( $Y_c/Y_t$ ) by the matrix tensile critical stretch. Then, the compressive fiber critical stretch value is obtained in a similar manner using iterative PD simulations of the notched laminated subjected to compressive loading and adjusting the compressive fiber critical stretch to obtain equivalent failure loads. Then, the calibrated compressive fiber critical stretch value can be used to obtain the tensile fiber critical stretch value using the ratio of tensile to compressive longitudinal strength of the lamina,  $X_t$  and  $X_c$ , respectfully. The entire process is repeated to fine-tune the calibration of the critical stretch values until the failure loads approach the measured values.

#### 4.3.2.1 Laminated plate with a center hole

The quasi-isotropic AS4/3501-6 carbon/epoxy composite laminates with a hole were previously considered by Wang et al. (2004). The layup for all of the composite panels is  $[45/0/-45/90]_{2s}$ . Each laminate specimen is 305 mm x 38.1 mm x 2.08 mm with a central through thickness hole. The specimen dimensions are shown in Fig. 29. Four different diameters (2.00, 3.81, 6.35, and 9.55 mm) of central holes are considered. The material properties of the lamina are  $E_{11} = 142$  GPa,  $E_{22} = 10.3$  GPa,  $G_{12} = 4.5$  GPa, and  $\nu_{12} = 0.27$ . The strength properties of the lamina are  $\sigma_{1t} = 2280$  MPa,  $\sigma_{1c} = -1440$  MPa,  $\sigma_{2t} = 57$  MPa,  $\sigma_{2c} = -228$  MPa, and  $\tau_{12} = 100$  MPa. The laminated specimens were tested to failure under both tensile and compressive loading in accordance with ASTM 3039 and SACMA SRM 3R standards, respectively.

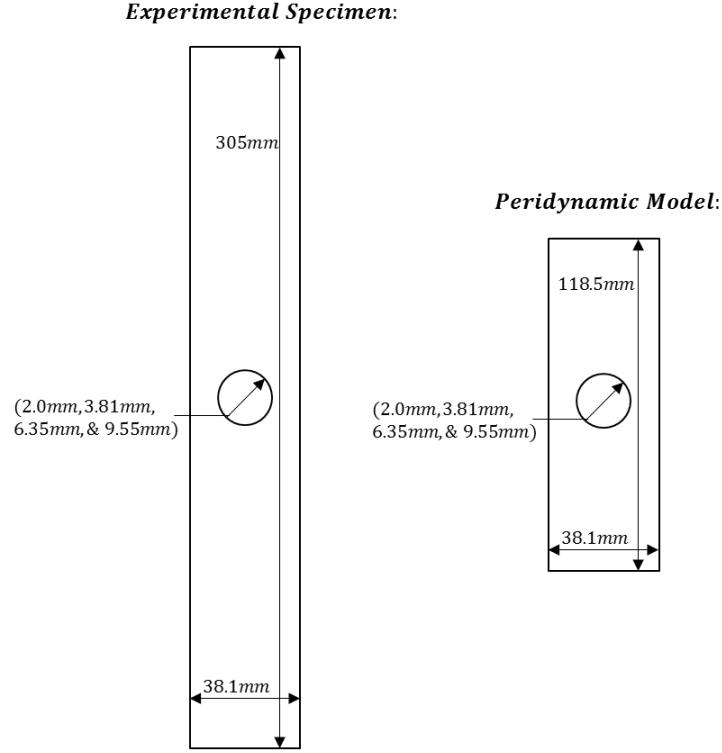


**Figure 29.** Dimension and loading conditions for notched quasi-isotropic AS4/3501-6 laminates.

The dimensions of each PD model are 118.5 mm x 38.1 mm with a total thickness of 2.08 mm as shown in Fig. 29. Each lamina is modeled with a grid of 156 material points in the length direction and 50 material points in the thickness direction; the grid spacing in the plane of the lamina is 0.76 mm. The horizon radius is specified as  $\delta = 3.015\Delta x$ . A central hole is added to each lamina by removing the material points falling within its specified diameter. The spacing in the thickness direction between each lamina is 0.13 mm. The loading is applied by specifying an end displacement at both the top and bottom edge of the model in incremental steps of 0.5 mm. Convergence for each step is ensured to enforce the quasi-static loading conditions.

The critical stretch parameters are obtained through the inverse approach by calibrating the experimentally observed peak failure loads to those obtained from the PD simulation. This calibration was completed on the specimen with a 6.35 mm diameter central hole. The tensile matrix critical stretch and compressive fiber critical stretch values are obtained through calibration with the tensile and compressive failure loads, respectively. The ratios of compressive strengths for a lamina are then used to determine the other critical stretch values. The critical stretch values obtained using the inverse approach are  $s_{cmt} = 0.0176$ ,  $s_{cmc} = -0.0528$ ,  $s_{cft} = 0.01882$ , and  $s_{cfc} = -0.01189$ . A PD simulation of a laminate with a 6.35 mm diameter central hole subjected to tensile loading is used to test the ability of these values to capture the failure load. The simulation predicted the initiation of failure at the central hole followed closely by an accumulation of damage throughout the entire laminate.

The peak loads obtained from the PD simulations are within 12% of the experimentally observed failure loads. Figure 30 shows the peak failure loads obtained from the PD simulations along with the experimentally results reported by Wang et al. (2004) for the four different hole diameters that were considered. A good agreement is observed between the experimental and the PD predicted peak failure loads for both the tensile and compressive tests.

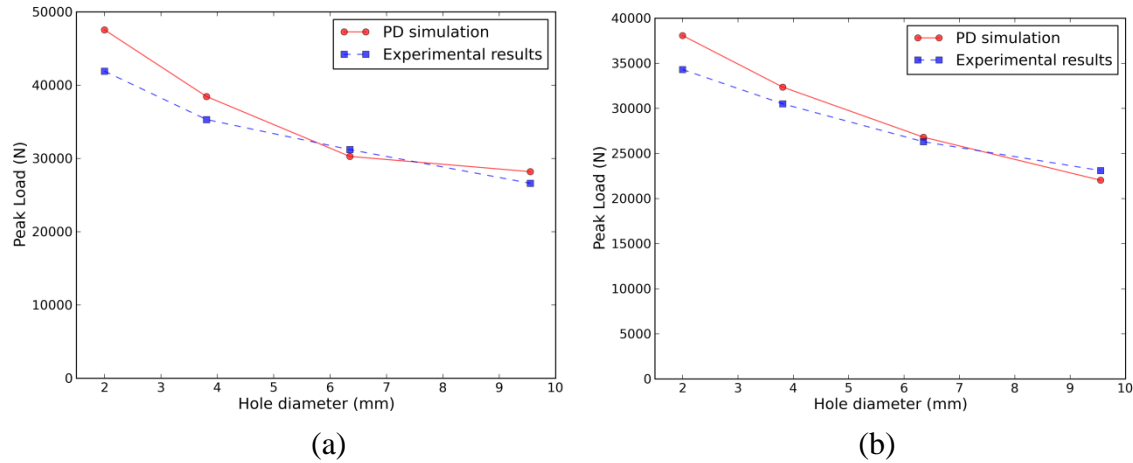


**Figure 30.** Experimental (Wang et al., 2004) and PD peak loads for a) tensile and b) compressive loading.

**Tensile Loading** - The final damage pattern transitions from one that is aligned with the  $45^\circ$  angle with respect to the principle coordinate system for the small diameter hole size, to the one aligned with the  $90^\circ$  angle for the larger hole sizes. Figure 31 shows the final damage patterns for each ply in the laminate composite subjected to a tensile load for four different central hole diameters. The specimen fracture pattern can be obtained by plotting the minimum damage at each material point in the thickness direction. The fracture for each of the specimens is plotted in Fig. 32. The resulting fracture pattern transition from a slant to a flat failure mode as the hole size increases. A similar observation shown in Fig. 33 was captured by Poon (1991) for carbon fiber epoxy specimens with the same base layup pattern and three times the thickness.

The initial tensile failure mode in all of the specimens is matrix cracking originating at both sides of the central hole in the  $90^\circ$  plies closest to the surface of the laminate. As the loading increases, the damage accumulates in all of the layers and propagates towards the edges of the plate. Delamination due to shear is observed between the layers near the surface. The amount of matrix and delamination that occurs depends on the size of the central hole. In the specimens with a large central hole, the amount of damage that accumulates is focused on either side of the hole. In the specimens with a small central hole, the area where damage occurs is extensive. The fiber failure occurs first in the  $0^\circ$  plies, followed quickly by the  $\pm 45^\circ$  layers. The peak load is observed with the initiation of the fiber failure.

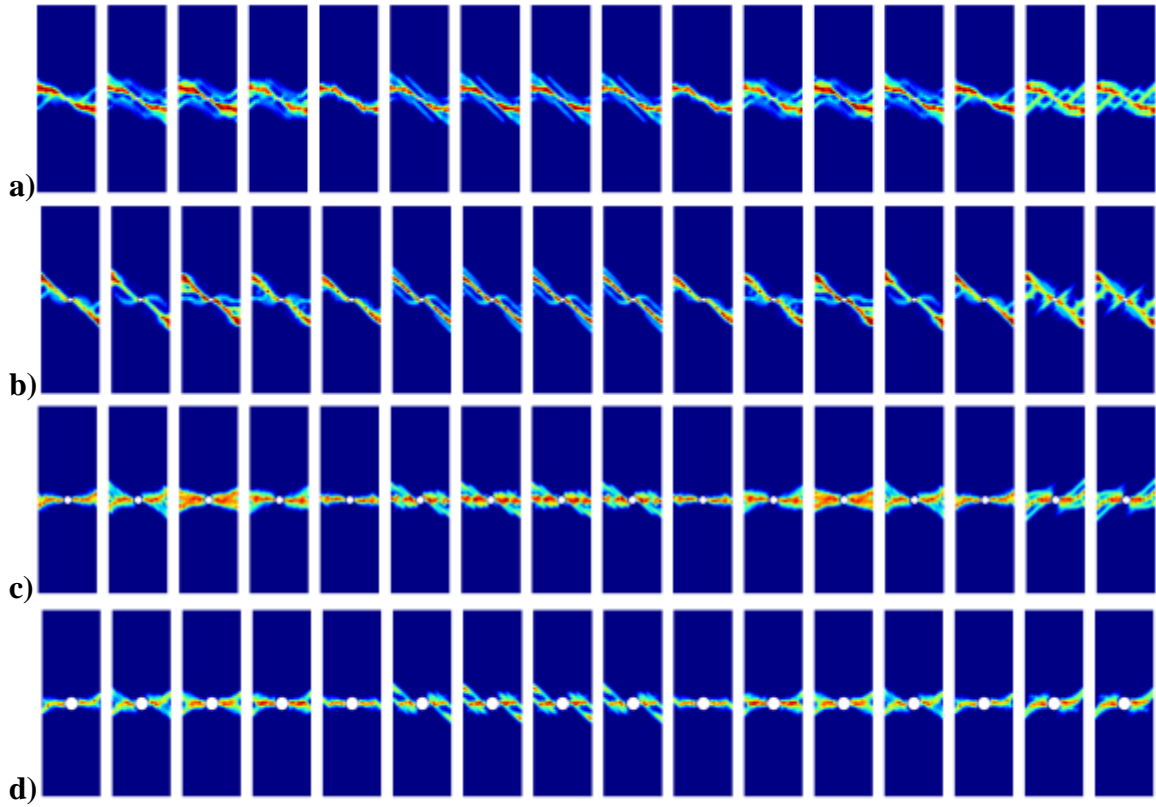


**Figure 31..** Failure patterns in each ply of a  $[45/0/-45/90]_{2S}$  laminate with a central hole of diameter a) 2.00 mm, b) 3.81 mm, c) 6.35 mm, and d) 9.55 mm subjected to tensile loading.

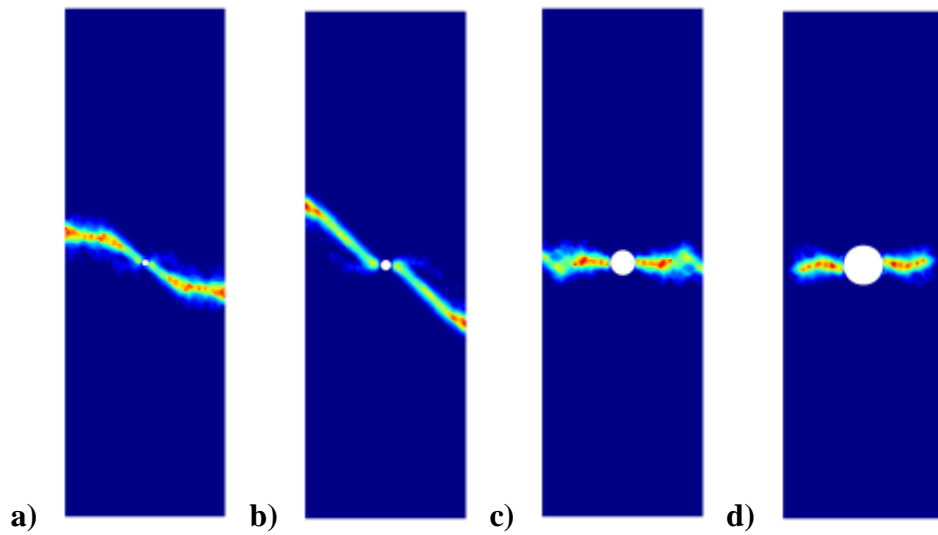


**Figure 32.** Failure patterns for a  $[45/0/-45/90]_{2S}$  laminate with a central hole of diameter a) 2.00 mm, b) 3.81 mm, c) 6.35 mm, and d) 9.55 mm subjected to tensile loading.

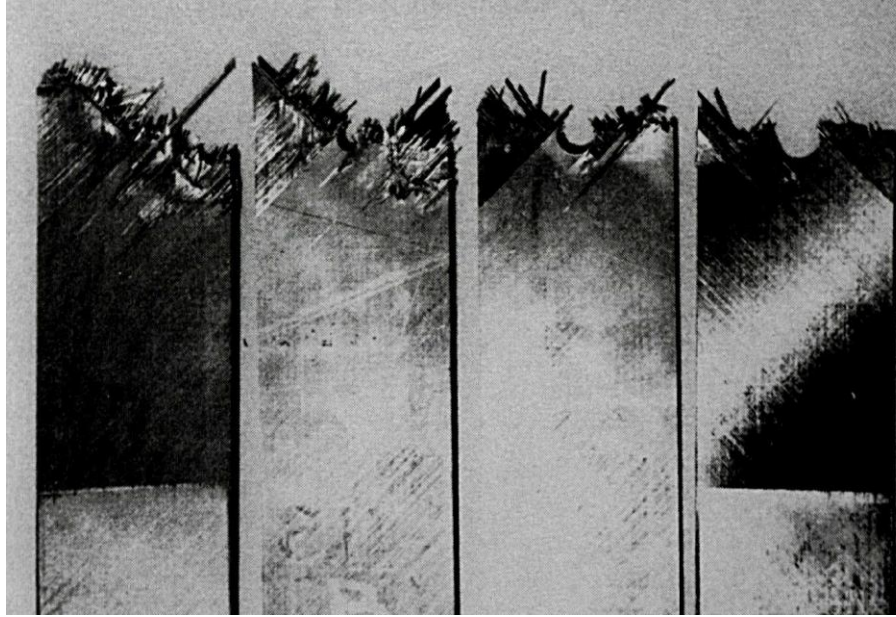


**Figure 33** Effect on failure patterns for a  $[45/0/-45/90]_{6S}$  laminate with a central hole of due to increase in hole size (Poon 1991).

**Compressive Failure** - Figure 34 shows the final damage patterns for each ply in the laminate composite subjected to a compressive load for the four different diameter central hole sizes considered. Due to quick propagation in the cases with the small diameter holes (2.00 mm and 3.81 mm), the final damage pattern is obtained at a time step long after the peak failure load. In all cases, the damage extends horizontally from the central hole toward the edge of the specimen. The final fracture pattern at each material point in the thickness direction is plotted in Fig. 35 for each of the different hole diameters. The fracture pattern is consistent for all the different hole diameters.

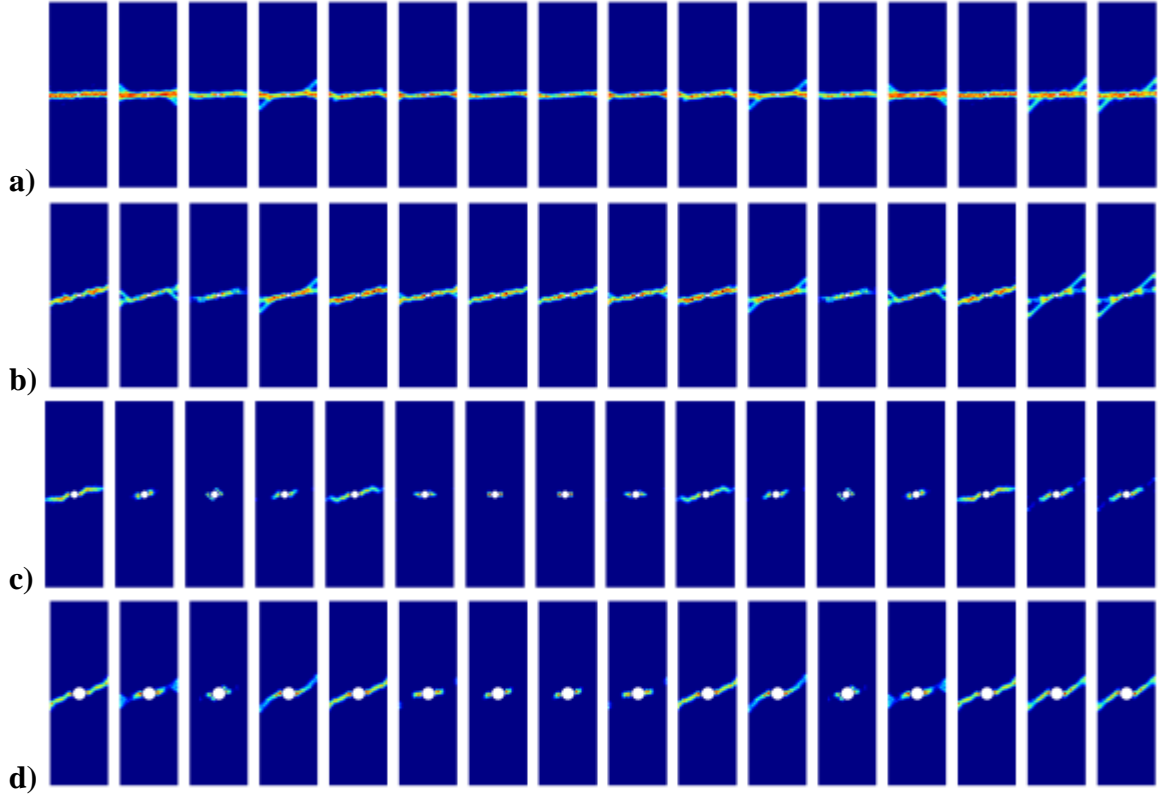


**Figure 34** Failure patterns in each ply of a  $[45/0/-45/90]_{2S}$  laminate with a central hole of diameter a) 2.00 mm, b) 3.81 mm, c) 6.35 mm, and d) 9.55 mm subjected to compressive loading.

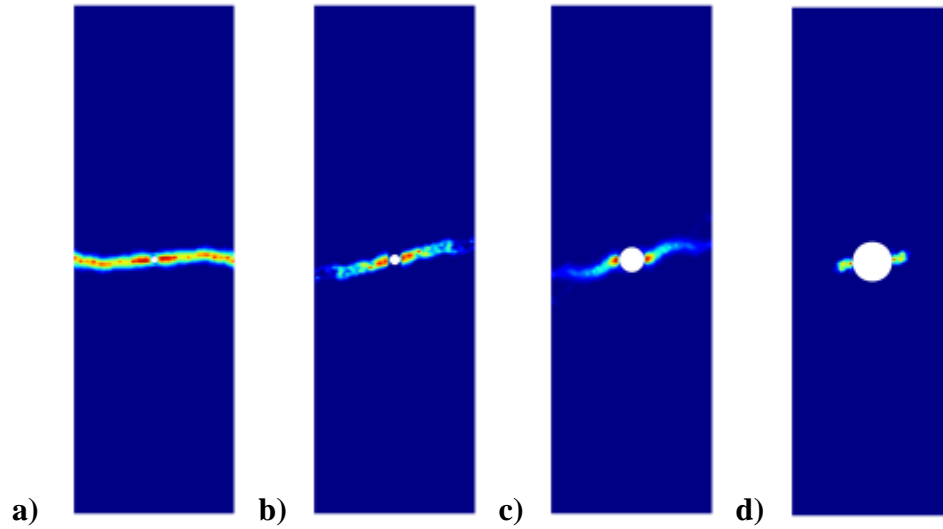


**Figure 35** Failure patterns for a  $[45/0/-45/90]_{2S}$  laminate with a central hole of diameter a) 2.00 mm, b) 3.81 mm, c) 6.35 mm, and d) 9.55 mm subjected to compressive loading.

The PD simulation for progressive failure can be compared with the experimental observations (Fig. 36) obtained by Suemasu et al. (2006). The initial damage observed in the PD simulation is fiber failure due to compression in the  $0^\circ$  layers followed by shear failure leading resulting in the loss of stiffness of the structure. This corresponds with the observations by Suemasu et al. (2006) of an the initial failure mode consisting of fiber micro-buckling in the  $0^\circ$  layers followed by delamination immediately before the failure of the specimen. The PD simulation also captures the damage extending horizontally from the hole that is observed in a C-scan of the experimental specimen immediately before the final failure of the specimen.

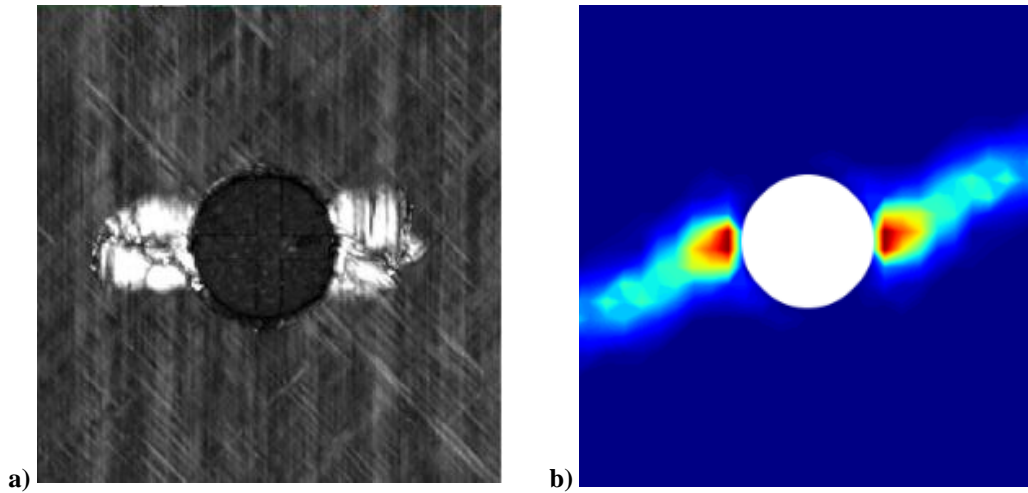


**Figure 36** a) C-Scan of the damage immediately before final failure (Suemasu et al., 2006), b) Failure pattern predicted using PD simulation.

## 5. Final remarks

This study demonstrates the ability of the PDLT to accurately capture the material response and progressive failure in composite laminates. PDLT correctly captures the structural response of laminates under various loading conditions and laminate layups. The capability of the PDLT to accurately model complex laminates is verified against the classical laminate theory and FEM.

The PDLT is able to capture matrix cracking, fiber breakage, and delamination due to transverse normal and transverse shear deformation. Also, the PD simulations using the critical stretch values obtained using the inverse approach are able to capture the residual strength of the notched specimens subjected to both tensile and compressive loading. The use of PD in this methodology allows the progressive damage of the composite structure to be captured in an extremely accurate manner.



## 6. References

Askari, A, Nelson, K., Weckner, O., Xu, J., and Silling, S., . "Hail Impact Characteristics of a Hybrid Material by Advanced Analysis Techniques and Testing." *Journal of Aerospace Engineering*, Vol. 24, 2011, pp. 210-217.

Askari, E., Xu, J., and Silling, S., "Peridynamic Analysis of Damage and Failure in Composites," In: 44th AIAA/ASME/ASCE/AHS/ASC Aerospace Sciences Meeting and Exhibit, Reno, NV, January 9-12, 2006, AIAA 2006-88.

Ayatollahi, M. R., and Aliha M. R. M., "Analysis of a New Specimen for Mixed Mode Fracture Tests on Brittle Materials." *Engineering Fracture Mechanics*, Vol. 76, 2009, pp. 1563-73.

Barenblatt, G.I., "The Mathematical Theory of Equilibrium Cracks in Brittle Fracture," *Advances in Applied Mechanics*, Vol. 7, 1962, pp. 104.

Barut, A., Madenci, E. and Tessler, A., "Prediction of Composite Laminate Strength Properties Using a Refined Zigzag Plate Element," 54th AIAA Structures, Structural Dynamics and Materials Conference, Boston, Massachusetts, 2013, AIAA Paper 2013-1539.

Belytschko, T., and Black, T., "Elastic Crack Growth in Finite Elements with Minimal Remeshing," *International Journal for Numerical Methods in Engineering*, Vol. 45, 1999, pp. 601-20.

Chang, F.K., and Chang, H.-Y., "A progressive damage model for laminated composites containing stress concentrations," *Journal Composite Materials*, Vol. 21, 1987, pp. 834–855.

Chang, F.K., and Lessard, L.B., "Damage tolerance of laminated composite containing an open hole and subjected to compressive loadings: part I – analysis." *Journal Composite Materials*, Vol. 25, 1991, pp. 2–43.

Colavito, K. W., Kilic, B., Celik, E., Madenci, E., Askari, E., and Silling, S., "Effect of Void Content on Stiffness and Strength of Composites by a Peridynamic Analysis and Static Indentation Test," In: 48th AIAA/ASME/ASCE/AHS/ASC Structures, Structural Dynamics, and Materials Conference, Honolulu, HI, April 23-26, 2007a, AIAA 2007-2251.

Colavito, K. W., Kilic, B., Celik, E., Madenci, E., Askari, E., and Silling, S., "Effect of Nano Particles on Stiffness and Impact Strength of Composites," In: 48th AIAA/ASME/ASCE/AHS/ASC Structures, Structural Dynamics, and Materials Conference, Honolulu, HI, April 23-26, 2007b, AIAA 2007-2021.

Dugdale, D.S. "Yielding of Steel Sheets Containing Slits," *Journal of the Mechanics and Physics of Solids*, Vol. 8.2, 1960, pp. 100-4.

W, Gerstle, N. Sau, and A. Silling, "Peridynamic modeling of plain and reinforced concrete structures," SMiRT18-B01-02, 8<sup>th</sup> International Conference on Structural Mechanics in Reactor Technology (SMiRT 18), Beijing, China, 2005.

Griffith, A. A., "The Phenomena of Rupture and Flow in Solids," *Philosophical transactions of the Royal Society of London*. A-221, 1921, pp. 163-198.

Hashin, Z. "Failure Criteria for Unidirectional Fiber Composites." *Journal of Applied Mechanics*, Vol. 47, 1980, pp. 329-334.

Hillerborg, A., Modeer, M., and Petersson, P. E., "Analysis of Crack Formation and Crack Growth in Concrete by Means of Fracture Mechanics and Finite Elements," *Cement and Concrete Research*, Vol. 6, 1976, pp. 773-81.

Hu, W., Ha, Y.D., and Bobaru, F., "Modeling Dynamic Fracture and Damage in a Fiber-Reinforced Composite Lamina with Peridynamics," *International Journal for Multiscale Computational Engineering*, Vol. 9, 2011, pp. 707-26.

Hu, W., Ha, Y. D. and Bobaru, F., "Peridynamic model for dynamic fracture in unidirectional fiber-reinforced composites," *Computer Methods in Applied Mechanics and Engineering*, Volumes 217–220, 2012, pp. 247-261.

Falzon, B.G., and Apruzzese, P., "Numerical analysis of intralaminar failure mechanisms in composite structures," Part I: FE implementation *Composite Structures*, Vol. 93, 2011, pp. 1039–1046.

B. Kilic, "Peridynamic theory for progressive failure prediction in homogeneous and heterogeneous materials," Ph.D. dissertation, Department of Aerospace and Mechanical Engineering, Univ. Arizona, Tucson, AZ, 2008.

Kilic, B., Agwai, A., and Madenci, E., "Peridynamic Theory for Progressive Damage Prediction in Center-Cracked Composite Laminates," *Composite Structures*, Vol. 90, 2009, pp. 141-151.

Kilic, B., and Madenci, E., "An Adaptive Dynamic Relaxation Method for Quasi-Static Simulations using the Peridynamic Theory," *Theoretical and Applied Fracture Mechanics*, Vol. 53, 2010, pp. 194-204.

Klein P. A., Foulk, J. W., Chen, E. P., Wimmer, S. A., and Gao, H. J., "Physics-based modeling of brittle fracture: Cohesive formulations and the application of meshfree methods," *Theoretical and Applied Fracture Mechanics*, Vol. 37, 2001, pp. 99-166.

Lapczyk, I., and Hurtado, J.A., "Progressive damage modeling in fiber-reinforced materials," *Composites: Part A*, Vol. 38, 2007, pp. 2333–2341.

Madenci, E., and Oterkus, E., *Peridynamic Theory and Its Applications*, Springer, Boston, MA, 2013.

Melenk, J. M., and Babuška I., "The Partition of Unity Finite Element Method: Basic Theory and Applications," *Computer Methods in Applied Mechanics and Engineering*, Vol. 139, 1996, pp. 289-314.

Moees, N., Dolbow, J., and Belytschko, T., "A Finite Element Method for Crack Growth without Remeshing," *International Journal for Numerical Methods in Engineering*, Vol. 46, 1999, pp. 131.

Ochoa, O.O. and Reddy, J.N., *Finite element analysis of composite laminates*. Kluwer Academic publishers, 1992.

Oterkus, E., Barut, A., and Madenci, E., "Damage Growth Prediction from Loaded Composite Fastener Holes by Using Peridynamic Theory," In: 51<sup>st</sup> AIAA/ASME/ASCE/AHS/ASC Structures, Structural Dynamics, and Materials Conference, Orlando, FL, 12-15 April, 2010, AIAA 2010-3026.

Oterkus, E., Madenci, E., Weckner, O., and Silling, S., "Combined Finite Element and Peridynamic Analyses for Predicting Failure in a Stiffened Composite Curved Panel with a Central Slot," *Composite Structures*, Vol. 94, 2012, pp. 839-850.

Oterkus, E. and Madenci, E., "Ordinary State-Based Peridynamic Material Constants," In: 53th AIAA/ASME/ASCE/AHS/ASC Structures, Structural Dynamics, and Materials Conference, Honolulu, HI, April, 2012, AIAA 2012-1946.

Poon, C. "Tensile Fracture of Notched Composite Laminates." No. IAR-AN-71. National Research Council of Canada Ottawa (Ontario) Institute for Aerospace Research, 1991.

Silling, S. A., "Reformulation of Elasticity Theory for Discontinuities and Long-range Forces," *Journal of the Mechanics and Physics of Solids*, Vol. 48, 2000, pp. 175-209.

S. A. Silling, "Dynamic fracture modeling with a meshfree peridynamic code," pp. 641-644, *Second MIT Conference on Computational Fluid and Solid Mechanics*, edited K. J. Bathe, Elsevier, Amsterdam, 2003.

S. A. Silling and E. Askari, "Peridynamic modeling of impact damage," pp. 197-205, *PVP-Vol. 489, Problems Involving thermal-Hydraulics, Liquid Sloshing, and Extreme Loads on Structures*, edited by F. J. Moody, American Society of Mechanical Engineers, 2004.

Silling, S. A., and Askari, E., "A Meshfree Method Based on the Peridynamic Model of Solid Mechanics." *Computers & Structures*, Vol. 83, 2005, pp. 1526-1535.

Silling, S. A., and Bobaru, F., "Peridynamic Modeling of Membranes and Fibers," *International Journal of Non-Linear Mechanics*, Vol. 40, 2005, pp. 395-409.

Silling, S. A., Epton, M., Weckner, O., Xu, J., and Askari, A., "Peridynamics States and Constitutive Modeling," *Journal of Elasticity*, Vol. 88, 2007, pp. 151-184.

S. A. Silling, M. Epton, O. Weckner, J. Xu, and A. Askari, "Peridynamics states and constitutive modeling," *J. Elast.* **88** (2007), 151-184.

Suemasu, H., Takahashi, H., and Ishikawa, T., "On Failure Mechanisms of Composite Laminates with an Open Hole Subjected to Compressive Load," *Composites Science and Technology*, Vol. 66, 2006, pp. 634-641.

Sun, C.T., *Strength Analysis of unidirectional composites and laminates*, Comprehensive composite materials. Elsevier Science 1, 2008, pp. 641–666.

Talreja, R., *Damage mechanics of composite materials*, vol.9. Elsevier Science Ltd, Oxford, 1994.

Wang, J., Callus, P. J., and Bannister, M. K., "Experimental and Numerical Investigation of the Tension and Compression Strength of Un-Notched and Notched Quasi-Isotropic Laminates," *Composite Structures*, Vol. 64, 2004, pp. 297-306.

Williams, M. L., "Stress Distribution at the Base of a Stationary Crack," *ASME Journal of Applied Mechanics* Vol. 24, 1957, pp. 109-114.

Xu, J., Askari, A., Weckner, O., Razi, H., and Silling, S., "Damage and Failure Analysis of Composite Laminates under Biaxial Loads," In: 48th AIAA/ASME/ASCE/AHS/ASC Structures, Structural Dynamics, and Materials Conference, Honolulu, HI, 2007, AIAA 2007-2315.

Xu, J., Askari, A., Weckner, O., and Silling, S., "Peridynamic Analysis of Impact Damage in Composite Laminates." *Journal of Aerospace Engineering*, Vol. 21, 2008, pp. 187-194.

Xu X. and Needleman A., "Numerical simulations of fast crack growth in brittle solids," *Journal of the Mechanics and Physics of Solids*, Vol. 42, 1994, pp. 1397-1434.